Coherent structure in the turbulent planar jet. Part 1. Extraction of proper orthogonal decomposition eigenmodes and their self-similarity

By S. V. GORDEYEV and F. O. THOMAS

Hessert Center for Aerospace Research, Department of Aerospace and Mechanical Engineering, University of Notre Dame, Notre Dame, IN 46556, USA

In this paper the coherent structure in the similarity region of the turbulent planar jet is examined experimentally by application of the proper orthogonal decomposition (POD). In particular, twin cross-stream rakes of X-wire probes are used to take cross-spectral measurements with different spanwise separations between the rakes and at several locations throughout the similarity region. The resulting POD spatial eigenfunctions for each of the three velocity components depend on cross-stream spatial coordinate, Strouhal number, and spanwise wavenumber. Corresponding eigenvalue distributions are obtained in Strouhal number–spanwise wavenumber space. Eigenvalue convergence is demonstrated to be rapid. When properly scaled the eigenfunctions and eigenvalues are shown to exhibit self-similarity though the streamwise location at which this commences depends on the particular velocity component. The results suggest that the flow supports a planar structure aligned in the spanwise direction as well as an essentially three-dimensional structure with asymmetrical shape in the cross-stream direction and pseudo-periodically distributed in the spanwise direction. Comparison of the single- and dual-rake implementations of the POD presented in this paper demonstrate that measurements confined to a single plane are incapable of properly extracting the planar modes. Rather, the single-rake implementation results in modes that appear to be a weighted sum of modes corresponding to different spanwise wavenumbers.

1. Introduction

In this paper the large-scale coherent structure in the similarity region of the planar turbulent jet is experimentally investigated by application of the proper orthogonal decomposition (POD). This work is focused upon the extraction and characterization of the POD eigenfunctions and associated eigenvalues and also addresses issues regarding their self-similarity. For our purpose in this paper, we consider a summation of the most energetic POD modes as synonymous with the term 'coherent structure'. In a follow-on paper, Part 2 (Gordeyev & Thomas 2000), we use a continuous wavelet transform in conjunction with the POD eigenmodes reported here to recover the instantaneous dynamics of the coherent structure. We regard this study as a first step in a longer term goal of developing a dynamical-system-based model of the planar turbulent jet flow field.

There are several reasons why we chose to examine the turbulent planar jet. It is

obvious that jet flows are technologically important in a very wide variety of applications. Further, the simple geometry and boundary conditions of the planar turbulent jet (in comparison with low-aspect-ratio rectangular, elliptic or even axisymmetric jets) make it attractive for fundamental investigations into turbulent flow structure. Finally, based upon previous experimental investigations to be described below, the similarity region of the planar turbulent jet has suggested the presence of large-scale organized motions. The evidence comes from two-point correlation measurements and conditional sampling techniques; certainly visualization by injection of a tracer reveals no evidence of underlying coherent structure in this fully turbulent flow. Although the self-similar axisymmetric jet has also shown evidence of large-scale coherent structure (see Tso & Hussain 1989), evidence suggests the structure in the planar jet is more well defined (or readily apparent). These factors taken in combination make the planar jet similarity region an attractive choice for the application of the proper orthogonal decomposition. Although the POD has been applied to the near field of the axisymmetric turbulent jet and the planar turbulent mixing layer (these studies are reviewed later in this section), to the authors' knowledge, this represents the first implementation of the POD in the planar jet flow field.

In this section of the paper, background material is presented which motivates the study and specific objectives of the experimental work are stated. Also presented is a brief review of previous studies focused on characterizing the turbulent planar jet similarity region as well as previous studies of jets and mixing layers that have utilized the POD.

1.1. *Background, motivation and objectives*

The concept of dynamically significant coherent vortical structures in turbulent flow has been with us for over fifty years. The term 'dynamically significant' implies that the coherent structures are expected to play important roles in processes such as scalar and momentum transport, chemical mixing and noise generation. Despite this generally acknowledged importance, the routine use of the coherent structure concept in turbulence modelling and flow control strategies has not yet been realized. In fact, the authors are unaware of any turbulence model in routine use which explicitly utilizes coherent structure dynamics. If one agrees that coherent structures are of dynamical importance to turbulent flow then it follows that they should be incorporated into turbulence modelling schemes, at least in some from.

Several experimental techniques have been developed for the extraction of the coherent structure from turbulent shear flows and these are reviewed by Bonnet & Delville (1996). Such techniques may be broadly classified as 'conditional' or 'non-conditional'. Conditional techniques involve sampling the flow only during those intervals of time that satisfy some predetermined criterion that is deemed dynamically significant and is related to the presence of the coherent structure that is sought. One drawback of these techniques is a lack of objectivity in the sense that one must have some predetermined idea regarding the structural topology in order to set the sampling criterion. In contrast, the proper orthogonal decomposition (POD) proposed by Lumley (1967) for investigation of the structure of inhomogeneous turbulent shear flows is an example of a non-conditional technique which is based on the two-point correlation tensor. The mathematical background to the POD is the Karhunen–Loève expansion as described in Karhunen (1946) and Loève (1955). The analysis of turbulent flow via the POD is the subject of a recent comprehensive review by Berkooz, Holmes & Lumley (1993) and the book by Holmes, Lumley & Berkooz (1996).

In an experimental context, the POD objectively extracts a complete set of spatial eigenfunctions (i.e. 'modes') from the measured second-order cross-correlation (or cross-spectral) matrix. The extracted modes serve as a set of optimal basis functions for expansion of the flow. The resulting expansion is optimal in the sense that convergence is more rapid than for any other possible basis. That is, the projection of the POD modes on the velocity field is maximized. It is generally recognized that the empirical eigenfunctions extracted by POD are intimately related to the coherent structure although the exact relationship is debated. For example, it was noted by Lumley (1981) that the first POD mode represents the coherent structure only if it contains a dominant percentage of the fluctuation energy. In other cases, POD modes give an optimal basis for flow decomposition but may have little to do with the physical shape of the underlying coherent structure. We choose to compromise and consider a summation of the most energetic POD modes as the large-scale coherent structure.

In order to obtain dynamical information regarding the coherent structure the empirically determined basis functions can be projected onto instantaneous realizations of the flow field. This allows the extraction of temporal phase coefficients for each of the modes that embodies their temporal behaviour. In order to preserve phase information (and thereby realize the full potential of this technique), rakes or meshes containing multiple probes (so-called 'multipoint measurements') are required. A comprehensive review of multipoint measurement techniques for turbulent flows and associated sampling requirements is presented by Glauser & George (1992).

Galerkin projection of a truncated subset of dominant POD modes onto the governing equations for the flow (i.e. the appropriately simplified version of the Navier–Stokes equations) provides a finite system of ODEs that one hopes will describe the essential physics of the flow. The influence of the truncated modes is typically modelled as a dissipative term that acts on the more energetic scales. The finite system of ODEs is solved to yield the temporal coefficients of the spatial POD modes. This provides the modelled flow field dynamics. Such an approach is attractive in that the essential dynamical mechanisms can be captured and implemented within the context of the well-developed mathematical techniques of dynamical systems and bifurcation theory. An excellent example of this approach is the work by Aubry *et al.* (1988) who successfully utilized the experimental POD eigenfunctions of Herzog (1986) to create a dynamical systems model of the near-wall region of a turbulent boundary layer. Using Galerkin projection of the experimentally determined POD modes onto the Navier–Stokes equation and performing suitable truncation, the model was found to simulate dynamical behaviour of turbulent boundary layers like the formation of streamwise rolls as well as intermittent ejection and burst-like events. A more recent, yet similar, pioneering effort to formulate a dynamical system model of the plane turbulent mixing layer is reported by Ukeiley & Glauser (1995).

Another unconditional extraction technique that is closely related to the POD is Linear Stochastic Estimation (LSE), Adrian (1977, 1979). LSE, like the POD, uses the cross-correlation matrix to extract structure from the flow. In Breteton (1992) it is shown that LSE can be treated as a weighted sum of an infinite number of POD modes. Therefore LSE provides a representation of the coherent structure in terms of a *single characteristic flow pattern*.

A primary objective of this study is to characterize the coherent structure in the similarity region of the planar turbulent jet via the POD. We seek to experimentally extract the POD eigenfunctions and eigenvalues. Particular attention is focused upon whether the POD modes and associated eigenvalues exhibit self-similar behaviour with

suitable scaling. Our interest in the turbulent plane jet is motivated, in part, by previous experimental studies that have suggested the existence of coherent structures in the similarity region. In order that the results of this investigation may be interpreted within the proper framework, these studies are next briefly described.

1.2. *Previous studies of coherent structure in the planar turbulent jet similarity region*

One of the first indications of large-scale structure in the plane turbulent jet was the 'jet flapping phenomenon' first reported by Goldschmitd & Bradshaw (1973) and later by Everitt & Robins (1978) and Cervantes & Goldschmidt (1981). This involved the observation of negative correlation between streamwise velocity fluctuations measured simultaneously by hot-wire probes placed on opposite sides of the jet centreline. The term 'flapping' is actually a misnomer which stems from early interpretations of this phenomenon in which it was suggested that the jet flaps much as a flag does. A lateral oscillation of the mean velocity profile was proposed as the cause of the negative time-average correlation. In contrast, Oler & Goldschmidt (1982) suggested that such correlation measurements are consistent with the presence of large-scale coherent structures in the similarity region of the planar jet in the form of a self-preserving antisymmetric array of counter-rotating spanwise vortices. Correlation measurements by Antonia *et al.* (1983) support such an antisymmetric structural array concept and showed that the apparent flapping could indeed be explained in terms of the passage of vortical structures past the fixed probe pair and was not associated with bulk lateral displacement of the jet. Antonia *et al.* (1983) also noted that the existence of an antisymmetric structural pattern was not in conflict with the earlier observations of both Gutmark & Wygnanski (1976) and Moum, Kawall & Keffer (1983) which showed the independent, three-dimensional random motion of the turbulent/non-turbulent interface on opposite sides of the jet.

Detailed iso-correlation contour maps based on both streamwise and lateral velocity fluctuations as obtained in different jet facilities by Mumford (1982), Antonia *et al.* (1986) and Thomas & Brehob (1986) exhibit a remarkable likeness and appear consistent with the existence of a large-scale structural array in the planar jet similarity region. The study by Antonia *et al.* (1986) was performed in a heated jet and the existence of laterally coherent temperature fronts was used as the basis for a conditional sampling scheme. The resulting coherent structure topology inferred from this method suggested an antisymmetric structural array. The temperature fronts were found to be associated with the diverging separatrix connecting adjacent structures on the same side of the jet. The contribution of the coherent and random motions to momentum and heat transport were found to be comparable.

Mumford (1982) used an iterative pattern recognition technique in order to in-vestigate the topology of the large-scale structure in the turbulent plane jet. An initial structural template, whose form was motivated by conventional correlation measurements, was convolved with experimental realizations of the flow and subse-quently modified as required by an optimization constraint until convergence was reached. The results suggested the existence of multiple roller-like structures whose axes extend in either the direction of mean flow homogeneity or in the direction of strain associated with the mean velocity gradient. The existence of multiple structural forms in the flow was suggested by Antonia *et al.* (1983) and Thomas & Brehob (1986) to account for the limited spanwise integral macroscales in the similarity region.

Space–time correlation functions formed between streamswise or lateral component velocity fluctuations measured simultaneously on opposite sides of the planar jet are

found to be quasi-periodic. As such, a local time scale, τ_c, may be defined as the average time delay between successive correlation function maxima or minima. Studies by Cervantes & Goldschmidt (1981), Antonia *et al.* (1983), Thomas & Goldschmidt (1986) and Thomas & Brehob (1986) in different test rigs all exhibit the same constant Strouhal number,

$$\frac{b}{\tau_c U_M} = 0.1, \tag{1.1}$$

where b is the local jet mean velocity half-width and U_M is the local jet centreline velocity. This suggests that the underlying large-scale component of the flow scales in accord with the requirements for global flow similarity, i.e. that $\tau_c \sim x^{3/2}$, where x is the streamwise spatial coordinate. More recent theoretical work performed by Ewing (1995) has shown that the equations governing the propagation of the two-point velocity correlation tensor in the planar jet admit self-similar solutions.

The convective velocity of the large-scale structural array has been estimated by Goldschmidt, Young & Ott (1981), Antonia *et al.* (1983) and Thomas & Brehob (1986) using a variety of two-point measurement techniques. These studies are in general agreement, suggesting that the large-scale structural array propagates at approximately 60% of the local centreline mean velocity.

Thomas & Goldschmidt (1986) considered the development of coherent structures throughout both the initial, interaction and similarity regions of the planar jet. The structures were noted to form and interact symmetrically in the transitional jet shear layers prior to the end of the potential core. Spanwise integral macroscales showed that the structures exhibit substantial two-dimensionality in the initial region. When the shear layers merged beyond the jet potential core, a restructuring of the flow was observed to occur which led to a loss in spanwise two-dimensionality on average and the formation of the self-preserving antisymmetric structural pattern described above. Antonia *et al.* (1983) also found that structures initially formed and interacted symmetrically in the initial region, with the shear layer interaction near the tip of the jet core triggering the formation and apparent dominance of the antisymmetric structural pattern downstream. The planar jet interaction region has been the focus of detailed studies by Weir, Wood & Bradshaw (1981) and Browne, Antonia & Chambers (1984). The latter study characterized the redistribution of turbulence quantities in the interaction region of the plane jet as 'dramatic' with a complex and violent interaction between initially symmetric jet shear layer vortices noted.

Although many details regarding the coherent structure's topology, origin, evolution, mutual interaction and role in the flow field dynamics are still unclear, there can be little doubt from the studies cited above that a significant coherent structure resides in the planar jet similarity region. Further, this structure appears to develop downstream of the shear layer interaction near the tip of the jet core. The resulting structural topology may well be complex since studies have suggested rollers aligned in both the spanwise direction and the direction of strain associated with the mean velocity profile.

1.3. *Previous applications of the POD in jet and mixing layer flows*

The POD was applied in the near field of a high Reynolds number axisymmetric jet shear layer in a study reported by Glauser (1987), Glauser & George (1989). This work demonstrated that the first POD eigenmode contained 40% of the kinetic energy while the first three eigenmodes accounted for approximately 80%. Based upon the POD results, a model for turbulence production in the axisymmetric shear

layer was developed which involves the interaction between two adjacent vortex ring structures shed from the nozzle lip. In a more recent study, Citrinniti (1996) revisited the axisymmetric jet shear layer at a fixed location 3 diameters downstream of the nozzle exit using an impressive polar array of 138 straight wire probes. The array was used to acquire instantaneous realizations of the flow in the (r, θ)-plane onto which the orthogonal eigenfunction basis was projected in order to obtain the temporal dynamics of the flow field. In general, the resulting dynamics were found consistent with those suggested by Glauser (1987).

A novel application of the POD was recently reported by Arndt, Long & Glauser (1997) who applied the technique to investigate the unsteady pressure field surrounding an axisymmetric jet. Since pressure is a scalar, there is a consequent simplification in the required measurements over those that involve the vector velocity field. Unlike most studies of free shear flows that employ the POD, the streamwise direction was considered inhomogeneous with the resulting eigenfunctions explicitly dependent on the streamwise coordinate. The shot-noise decomposition was used to define characteristic dynamic events that were found to involve mergings of both two and three vortices.

The application of the POD to investigate coherent structure in the planar mixing layer is the topic of works by Delville, Bellin & Bonnet (1990), Delville (1993, 1994), Ukeiley & Glauser (1995), Bonnet & Delville (1996), and Delville *et al.* (1999). In the work by Delville *et al.* (1999) it was found that 70% of the mean-square fluctuation energy was contained within the first three eigenmodes. The studies also contrasted the results from scalar and vectorial applications of the POD. Using twin rakes of X-wires, the large-scale structure in the asymptotic region of the planar mixing layer was investigated by Ukeiley & Glauser (1995). The measurements were performed at $x/\delta_\omega = 21.7$, where x is the streamwise coordinate and δ_ω is the vorticity thickness. This study is of particular relevance to the work reported here since the geometric similarity between the planar mixing layer and planar jet (at least at a superficial level) warrants a similar experimental approach in implementing the POD. Ukeiley & Glauser (1995) found that the energy in the POD modes rapidly converges, with 49% contained in the first mode. The first mode exhibited evidence of both streamwise and spanwise oriented vortices. The Galerkin method was used to project the empirical basis functions on the Navier–Stokes equations thereby providing a truncated system of ODEs for the temporal coefficients which were examined within the context of dynamical systems theory.

1.4. *Objectives and organization*

In the following sections of this paper we present the results of an experimental investigation aimed at extracting the spatial POD eigenfunctions and associated eigenvalues in the planar turbulent jet similarity region. Motivated by the theoretical work of Ewing (1995), we investigate whether the POD modes exhibit self-similarity. Strictly speaking, the results of Ewing (1995) are a necessary but not sufficient condition for self-similarity of the POD modes. The resulting structure inferred from our experiments will be discussed as are the possibilities of implementing the results in constructing a dynamical model of the planar jet similarity region. In Part 2 a continuous wavelet transform method is used in conjunction with the spatial POD modes described here to obtain the instantaneous topology and dynamics of the coherent structure in the jet similarity region.

The following section describes the planar jet flow field facility. This section also contains a detailed description of the experimental implementation of the POD. The
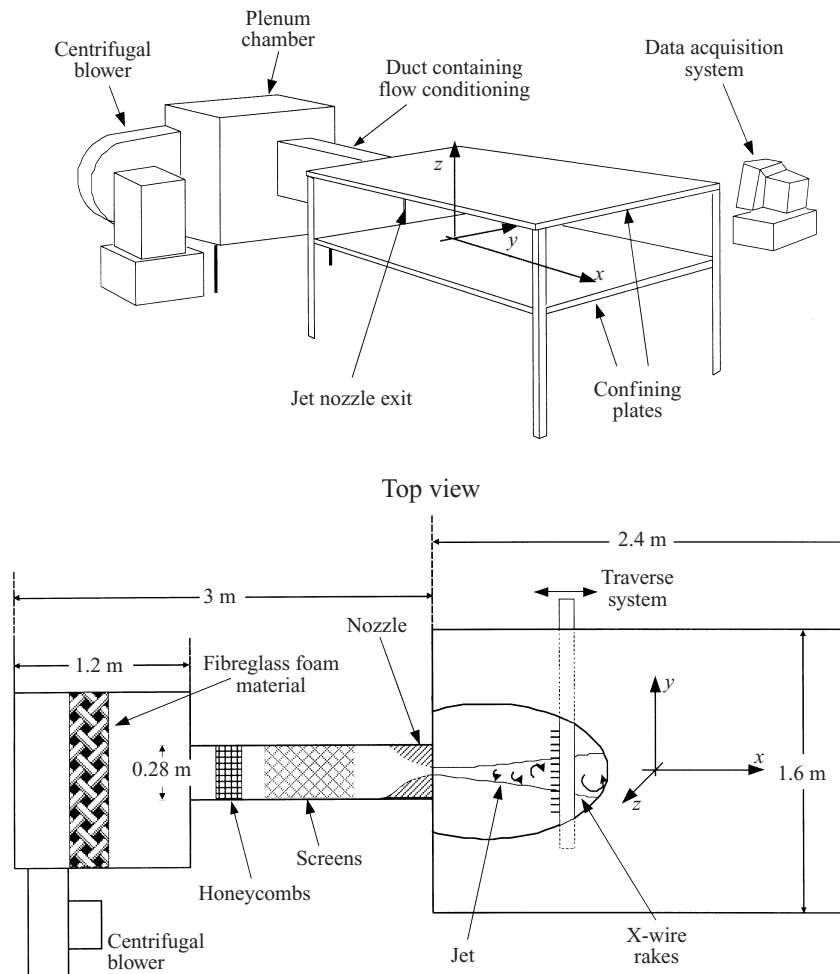
FIGURE 1. Schematic of the turbulent planar jet flow field facility.

experimental results are summarized and arguments related to similarity scaling of the eigenvalues and eigenfunctions are presented in §3. The paper concludes with a discussion regarding the implications of the experimental results in §4.

2. Description of the experiment

2.1. *Experimental facility and instrumentation*

All the experiments were conducted in the planar jet flow field facility located at the Hessert Center for Aerospace Research at the University of Notre Dame. A schematic of the jet flow field facility is shown in figure 1. The flow is driven by a centrifugal blower that supplies air to a cubic plenum chamber with dimensions of 1.2 m per side. Inside the plenum the air is forced to diffuse through a large layer of porous fibreglass insulation material which serves to both filter the air and decouple the flow from any blower pulsation. After leaving the plenum, the air enters a rectangular flow conditioning duct that leads to the nozzle assembly. The duct contains a section of honeycomb flow straighteners and a series of turbulence-reducing screens of various mesh sizes. The jet is formed by a two-dimensional nozzle contraction that was

constructed from aircraft foam which was then laminated with an acrylic material in order to achieve a smooth and polished finish. The nozzle contraction takes the form of a cubic polynomial contour with zero-derivative end conditions. The nozzle has a contraction ratio of $16:1$ and ends in a two-dimensional slot that is $D = 1.27$ cm in width and $H = 45.7$ cm in height giving an aspect ratio (height/width) of $36:1$. It is in the longer dimension that the nozzle walls are contoured while the shorter dimension walls are flat. From the nozzle the air discharges to the surrounding ambient environment. The flow field is formed between two horizontal confining plates of dimension 2.5 m in the flow direction and 1.61 m in width which serve to keep the base flow two-dimensional in nature. Twin sheet metal face plates mounted flush with the nozzle exit plane extend laterally to the edge of the flow field and ensure that entrained air enters the near field of the jet with negligible axial momentum component. All other sides of the flow field remain open. The entire setup is supported in a sturdy angle iron frame to which a computer controlled traversing mechanism is attached which provides precise hot-wire probe positioning in the three coordinate directions. A series of large screens surround the jet flow field facility in order to ensure that any laboratory air circulation has minimal effect on the flow. It should be noted, however, that the jet was operated in a large laboratory space (353 m^2 floor area) so that any such effects were exceedingly small.

In this paper x will denote the streamwise spatial coordinate which is made non-dimensional by the nozzle slot width, D. The cross-stream spatial coordinate is y and is made non-dimensional by the local mean velocity half-width, $b(x)$. The half-width is defined as the distance from the jet centreline to the lateral location where the local mean velocity has fallen to one-half its centreline value. The spanwise spatial coordinate extending in the direction of mean flow homogeneity is denoted z. The origin of the spanwise z-axis is chosen in the centreplane midway between the two flow field confining plates, with positive direction upward. The velocity components corresponding to x, y, z are denoted u, v, w, respectively.

The nozzle exit velocity was $U_0 = 35$ m s^{-1} with a corresponding Reynolds number based on nozzle slot width of $Re_D = 28\,000$. The initial jet mean velocity profiles are flat (i.e. a 'top-hat' shape) with the mean velocity variation across the nascent jet shear layers closely approximated by a classic hyperbolic tangent type of profile. The free shear layers at the nozzle lip are both laminar and have an initial momentum thickness $\theta_0 = 0.12$ mm. The initially most amplified jet shear layer instability frequency occurs near the Strouhal number $St_\theta = 0.033$ based on the mean speed across the layer and the initial momentum thickness. This corresponds to a frequency of approximately 4.8 kHz.

The planar turbulent jet flow field consists of three distinct regions. In the initial region closest to the nozzle exit the jet consists of two transitioning planar shear layers (with velocity ratio of unity) which bound a central core of irrotational flow (known as the potential core). As a result of sequential vortex pairing events and the associated mixing transition, the shear layers widen with downstream distance and the potential core is engulfed near $x/D \approx 4$. The near field of the planar jet is unique in that the shear layers on opposite sides of the centreline contain large-scale, spanwise-coherent vorticity of opposite sign. The merging of the shear layers near the tip of the jet potential core gives rise to a complex interaction region which extends to approximately $x/D = 10$ where the jet begins to reach a state dynamical equilibrium and the mean velocity profiles begin to exhibit evidence of self-similar behaviour. In other words, the mean velocity profiles become congruent when scaled by the local centreline velocity $U_M(x)$ and the local mean velocity half-width $b(x)$.
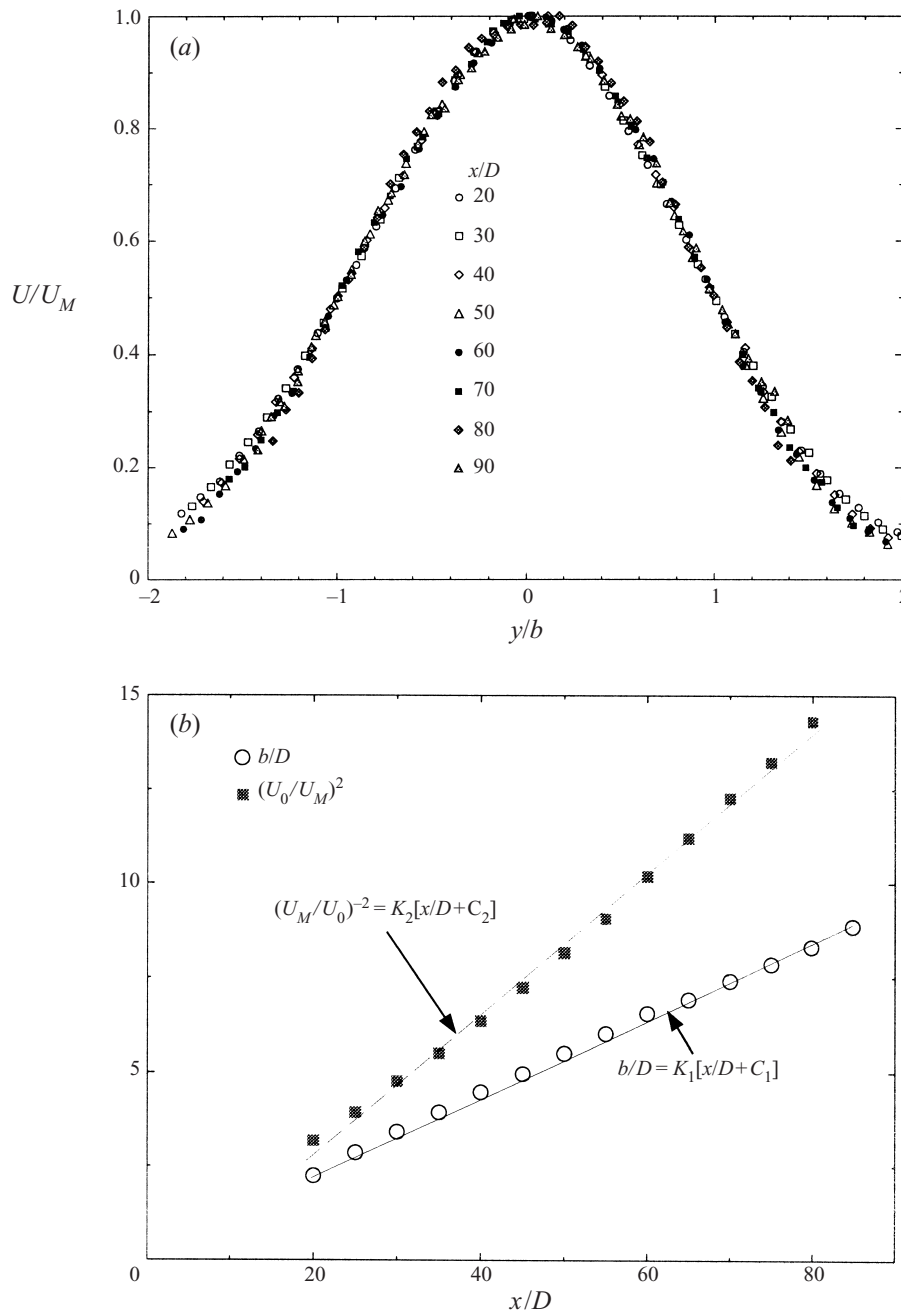
FIGURE 2. (*a*) The cross-stream variation of the normalized mean *u*-component velocity, (*b*) streamwise variation of the local half-width b/D and the local maximum velocity U_M.

Figure 2(*a*) presents mean velocity profiles measured at several streamwise locations in the jet. The collapse of the profiles in the similarity coordinates $\overline{U}/U_M$ versus y/b is apparent. Figure 2(*b*) summarizes the streamwise variation of both the mean velocity half-width, $b(x)$, and the centreline velocity, $U_M(x)$ for the jet under investigation here. For $x/D > 10$ both quantities exhibit classic similarity scaling with $b(x)$ well

approximated by

$$\frac{b}{D} = K_1 \left[\frac{x}{D} + C_1 \right], \tag{2.1}$$

with the measured *widening rate*, $K_1 = 0.1$, and the *geometric virtual origin* given by $C_1 = 0.071$. The local centreline velocity variation closely follows,

$$\left(\frac{U_M}{U_0} \right)^{-2} = K_2 \left[\frac{x}{D} + C_2 \right], \tag{2.2}$$

with the measured *mean velocity decay rate*, $K_2 = 0.22$, and the *kinematic virtual origin* $C_2 = -0.18$. These values of K_1 and K_2 are quite typical of those found in the literature (see Chu 1993 for a compilation of values). Published values for the virtual origins show considerable scatter and the study by Flora & Goldschmidt (1969) has shown them to be strong functions of flow field initial conditions.

It is well known that profiles of various turbulent moments typically require larger streamwise distances for the onset of self-similar behaviour than does the mean velocity. Figure 3(*a*) presents profiles of the scaled Reynolds stress $-\overline{u'v'}/U_M^2$ versus y/b obtained at representative streamwise locations in the planar jet. Also shown for comparison are the Reynolds stress measurements of both Gutmark & Wygnanski (1976) and Bradbury (1965). The Reynolds stress is also compared with that calculated from the measured mean velocity profile shown in figure 2(*a*) and the thin shear layer form of the momentum equation. The agreement is quite good for $y/b < 1$. Outside this region a disparity between stress profiles is noticeable, and is most likely associated with intermittency effects near the edge of the jet. Figure 3(*b*) presents measured profiles of scaled streamwise and lateral-component fluctuation intensities at several representative streamwise locations. From these measurements (and others that are not presented here) it was concluded that self-similarity for second-order statistics starts at approximately $x/D = 50$. Since the focus of this research is on coherent structure in the similarity region, the POD measurements were performed within the streamwise interval $50 \leqslant x/D \leqslant 90$. Although the jet facility allows measurements to be made at larger x/D, the low velocities associated with these stations give rise to larger relative uncertainties in multi-component hot-wire measurements. The streamwise range quoted above represents an optimum in the sense of achieving both self-similar jet behaviour and minimal measurement uncertainty.

The experimental implementation of the POD requires the measurement of the spatial cross-correlation tensor at selected x/D locations throughout the similarity region of the jet. The process of obtaining the cross-correlation tensor is expedited by the use of cross-stream rakes of probes. This also allows one to obtain simultaneous velocity–time histories at multiple lateral locations across the jet which is essential later if one is to reconstruct the temporal dynamics of the extracted POD eigenfunctions.

In this paper results from two types of experiments are reported. The primary 'two-rake experiment' involves correlation measurements involving all three fluctuating velocity components at selected x/D planes in the similarity region of the jet as obtained by means of two spanwise-separated rakes of eight X-wire probes each. Both of the rakes are located at the same x/D location and are oriented in the cross-stream direction, parallel to each other. The two rakes are separated in the spanwise direction by a user-selected distance Δz. The rakes are mounted on a computer-controlled traverse system which allows both their relative spanwise separation and mutual streamwise position to be controlled. In contrast, the 'one-rake experiment'
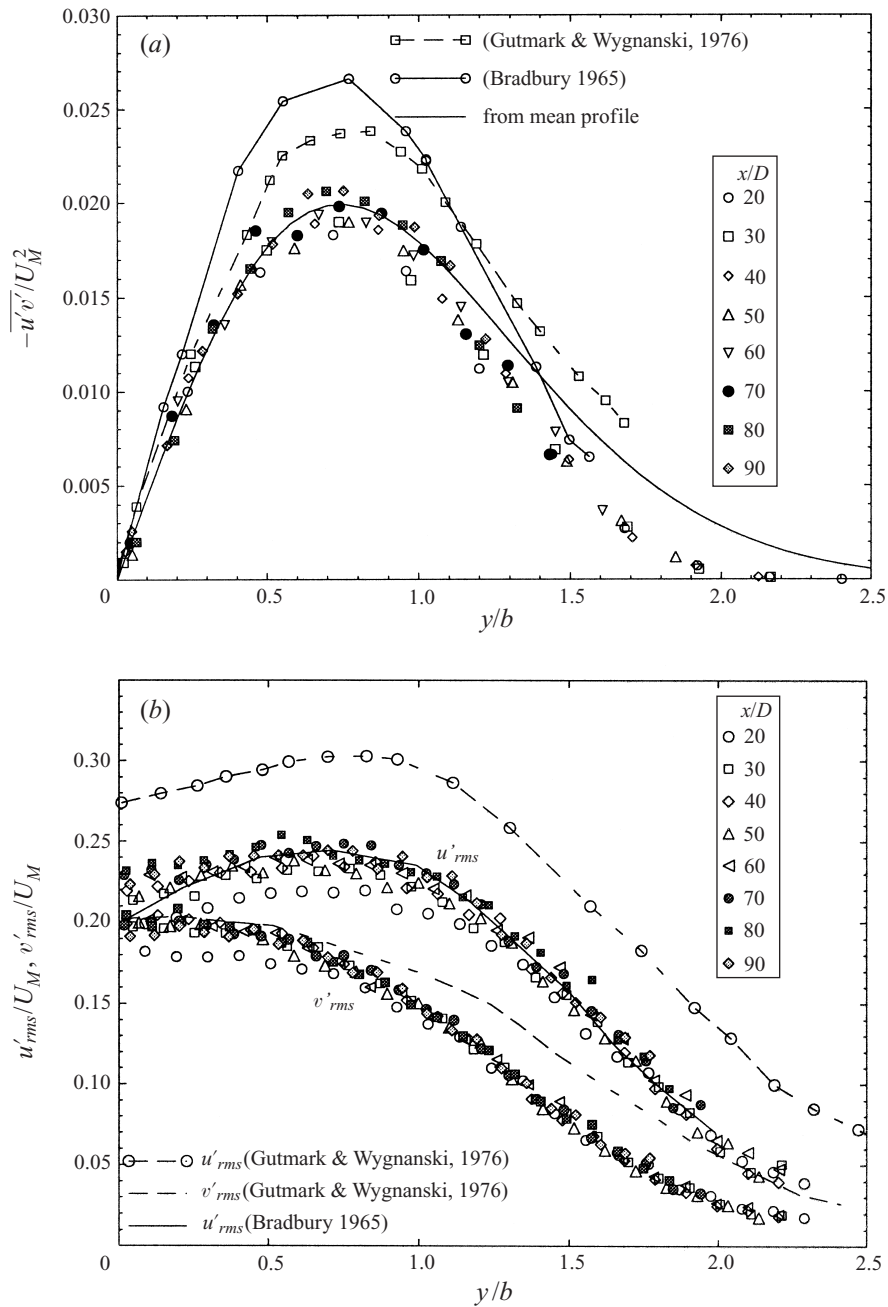
FIGURE 3. The normalized (*a*) Reynolds stress $-\overline{u'v'}(x,y)/U_M^2(x)$ and (*b*) $u'_{rms}(x,y)/U_M(x)$ and $v'_{rms}(x,y)/U_M(x)$.

involved a single cross-stream rake of 16 X-wire probes. At each streamwise location investigated, this measurement was confined to a single line extending in the cross-stream direction. The one-rake experiment was performed in support of the two-rake experiment. By doubling the number of probes in the *y*-direction it allowed an assessment of the degree of spatial aliasing in the inhomogeneous coordinate.

In addition, since many previous studies of the planar turbulent jet have focused on measurements in a fixed (x, y)-plane, it seems appropriate to compare POD eigenmodes extracted from the one- and two-rake experiments. Details regarding both experiments are presented in §§ 2.2 and 2.3.

Lateral profiles of turbulent normal and Reynolds stresses made both with a single X-wire probe in the flow and with each of the multi-probe rakes were found to be virtually identical. This indicated that the blockage associated with the rakes and associated support hardware had no detectable effect on the measurements.

Each of the rakes utilizes miniature X-wire probes fabricated by Auspex Corporation (types A55P61 or AHWX-100). These X-wire probes have a 0.9 mm spacing between the two probe sensors and a sensor wire length of 0.8 mm. The probe shaft lies in the plane of the X array. The required 32-channels of constant-temperature hot-wire anemometry and associated anti-alias filters were fabricated in-house. The dynamic response of the transducers was found to be flat to 50 kHz, which will be shown to be more than sufficient for the needs of the experiments. The anti-alias filtered output voltages from the hot wires were simultaneously sampled and digitized by means of a 64-channel MSXB data acquisition system made by MicroStar Laboratories. This system features multiple sample-and-hold cards and a high-speed A/D board that is capable of simultaneously sampling the 32 hot-wire anemometer output voltages at rates up to 50 kHz with no detectable phase lag between channels. Digital data are logged to an external drive in binary format and pre-processed on a laboratory PC computer. The data were subsequently uploaded to a Sun SPARCstation 30 for post-processing.

The X-wires were calibrated in the planar jet flow field facility by means of a small removable rotating table which simultaneously placed all of the X-wires into the potential core near the nozzle exit of the planar jet. The table pivots the probes about an axis passing through the centre of the X-array and thereby allows one to set a given angle between the probe axis and the oncoming uniform flow. During calibration the speed of the jet was set to 12 different values within the range from 0 to U_0 as measured by a Pitot-static probe connected to a U-tube micromanometer. The probe angle with respect to the oncoming flow was set to 11 different values within the range of $-45°$ to $+45°$. The output voltage from each anemometer was recorded for each velocity–flow angle combination. These data were used to create a look-up table to compute velocity vectors from the voltages measured during the experiment. The look-up table procedure used in this study is similar to that described in Chu (1993) and Ukeiley & Glauser (1995).

2.2. *Description of the two-rake experiment*

In this section we describe the basic procedure by which the POD eigenmodes and associated eigenvalues are extracted in the two-rake experiment. Due to a similarity in basic flow field geometries, our approach is patterned after that developed and successfully implemented by Ukeiley & Glauser (1995) and Delville *et al.* (1999) for their study of the plane mixing layer.

Figure 4 presents a schematic and photograph of the two X-wire rakes in the planar jet facility. Using the rakes, correlation measurements involving the (u, v) and (u, w) velocity components are performed at several planes of constant x/D over the streamwise range $50 \leqslant x/D \leqslant 90$. We denote the cross-correlation tensor as

$$R_{\alpha\beta}(y, y', z, z', t, t') = \langle u_\alpha(y, z, t) u_\beta(y', z', t') \rangle, \tag{2.3}$$

where $\langle \cdot \rangle$ denotes an ensemble average and Greek subscripts denote a fluctuating

Schematic

X-wire rake

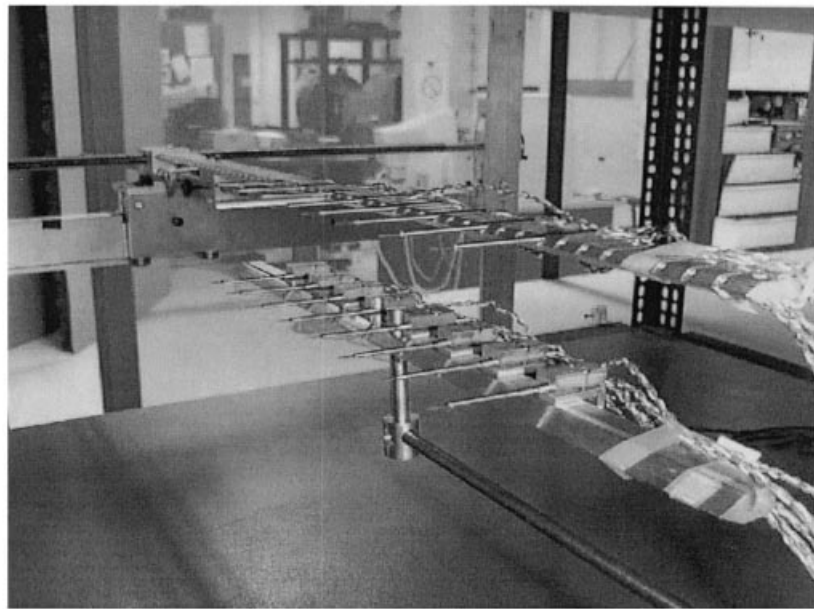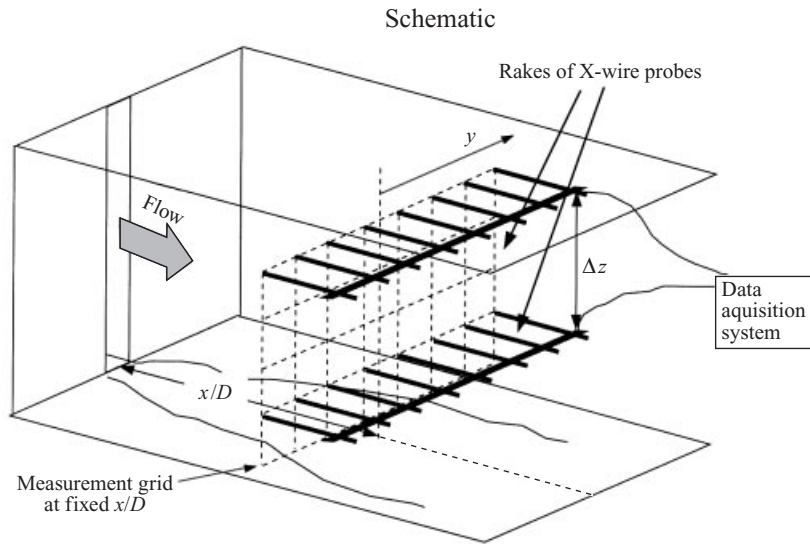FIGURE 4. Orientation of the X-wire probe rakes in the two-rake experiment.

velocity component u, v or w. The velocity measurement $u_\alpha(y, z, t)$ corresponds to the first rake and $u_\beta(y', z', t')$ corresponds to the second. Note that the X-wire probes are capable of the simultaneous measurement of either ($\alpha = u$, $\beta = v$) or ($\alpha = u$, $\beta = w$). Because the flow is stationary in time and is assumed homogeneous in the spanwise direction (z), the cross-correlation matrix $R_{\alpha\beta}(y, y', z, z', t, t')$ depends on the relative coordinates $\Delta z = z - z'$ and $\tau = t - t'$.

Since time is a homogeneous direction, we perform a temporal Fourier transform

of $R_{\alpha\beta}$, in order to obtain the cross-spectral matrix,

$$S_{\alpha\beta}(y, y', \Delta z, f) = \int R_{\alpha\beta}(y, y'\Delta z, \tau) e^{-2\pi i f \tau} \, d\tau. \tag{2.4}$$

Actually the cross-spectral matrix $S_{\alpha\beta}(y, y', \Delta z, f)$ can be computed directly from Fourier transformation of the individual velocity–time histories (see Bendat & Piersol 1986) and that is the approach taken in this investigation. Hence we have the equivalent relation,

$$S_{\alpha\beta}(y, y', \Delta z, f) = \lim_{T \to \infty} \frac{1}{T} \langle \hat{u}_\alpha^*(y, z, f) \hat{u}_\beta(y', z + \Delta z, f) \rangle \tag{2.5}$$

with $\hat{u}_\alpha(y, z, f) \equiv \int_0^T u_\alpha(y, z, t) \exp(-2\pi i f t) \, dt$ denoting the Fourier transformation of the velocity vector for each block, T is the total time duration of the data block and the asterisk denotes a complex conjugate. We next perform a *spatial* Fourier transformation in the homogeneous z-direction which provides a spanwise wavenumber-dependent cross-spectral matrix,

$$\Phi_{\alpha\beta}(y, y'; f, k_z) = \int S_{\alpha\beta}(y, y', \Delta z, f) e^{i k_z \Delta z} \, d(\Delta z), \tag{2.6}$$

where k_z is a spanwise wavenumber. As shown in Lumley (1970), the spectral correlation tensor $\Phi_{\alpha\beta}(y, y'; f, k_z)$ will be a kernel in the integral equation to find the POD modes for different frequencies f, and spanwise wavenumbers, k_z,

$$\int \Phi_{\alpha\beta}(y, y'; f, k_z) \phi_\beta^{(n)}(y'; f, k_z) \, dy' = \lambda^{(n)}(f, k_z) \phi_\alpha^{(n)}(y; f, k_z). \tag{2.7}$$

Here superscript n denotes mode number. The solution of (2.7) gives a complete set of orthonormal eigenfunctions $\phi_\alpha^{(n)}(y; f, k_z)$ with corresponding positive eigenvalues $\lambda^{(n)}(f, k_z)$. Note that the resulting eigenfunctions depend on temporal frequency, spanwise wavenumber and lateral position in the inhomogeneous direction. Any velocity realization can be represented as a sum of the eigenfunctions

$$u_\alpha(y, z, t) = \sum_{n=1}^{\infty} \iint c^{(n)}(f, k_z) \phi_\alpha^{(n)}(y; f, k_z) \exp(2\pi i f t) \exp(i k_z z) \, df \, dk_z. \tag{2.8}$$

In (2.8) the coefficients $c^{(n)}(f, k_z)$ are obtained by projection of the eigenmodes onto individual realizations of the flow field. Although this aspect is not considered further here, the interested reader is referred to Gordeyev (1999) for details. The spectral correlation tensor $\Phi_{\alpha\beta}(y, y'; f, k_z)$ can be expanded as

$$\Phi_{\alpha\beta}(y, y'; f, k_z) = \sum_{n=1}^{\infty} \lambda^{(n)}(f, k_z) \phi_\alpha^{(n)}(y; f, k_z) \{\phi_\beta^{(n)}(y'; f, k_z)\}^*. \tag{2.9}$$

Finally, the eigenvalues $\lambda^{(n)}(f, k_z)$ represent the energy distribution in frequency–spanwise wavenumber space for each of the extracted POD modes. From the above discussion, it is apparent that the problem of finding the POD modes is reduced to solving a number of integral equations (2.7) with f and k_z as parameters.

Before considering details regarding the practical implementation of the above relationships, it is useful to point out certain symmetries possessed by the cross-spectral tensor when measured in the planar jet flow field. By the term 'symmetries' we mean certain transformations of the physical variables which leave the flow invariant.

Consideration of these symmetries leads to a simplification of the experiment. The particular symmetries in the planar jet worth mentioning are the following.

(*a*) Invariance with respect to translations in both homogeneous directions: time and z-direction.

$$t \rightarrow t + \text{const}, \qquad z \rightarrow z + \text{const}. \tag{2.10}$$

This property was used to simplify the multi-dimensional integral equation,

$$\iiiint R_{\alpha\beta}(\boldsymbol{x}, \boldsymbol{x}', t, t') \phi_{\beta}^{*}(\boldsymbol{x}', t') \, \mathrm{d}\boldsymbol{x}' \, \mathrm{d}t' = \lambda \phi_{\alpha}(\boldsymbol{x}, t) \tag{2.11}$$

to a number of one-dimensional integrals (2.7).

(*b*) Reflections in the z-direction,

$$z \rightarrow -z, \; u \rightarrow u, \; v \rightarrow v, \; w \rightarrow -w. \tag{2.12}$$

Application of (2.12) to (2.5) gives the following property of the cross-spectral matrix $S_{\alpha\beta}$:

$$S_{\alpha\beta}(y, y', \Delta z, f) = \pm S_{\alpha\beta}(y, y', -\Delta z, f), \tag{2.13}$$

where the minus sign should be chosen if either α or β is equal to w, but not both. This symmetry allows one to restrict the measurements of the S-matrix to positive Δz only, which reduces the required data collection at a given streamwise location by a factor of two.

(*c*) Physical symmetry in the y-direction,

$$y \rightarrow -y, \; u \rightarrow u, \; v \rightarrow -v, \; w \rightarrow w$$

leads to the following equality:

$$S_{\alpha\beta}(y, y', \Delta z, f) = \pm S_{\alpha\beta}(-y, -y', \Delta z, f). \tag{2.14}$$

The minus sign is chosen if α or β is equal to v. Equation (2.14) says that the $S_{\alpha\beta}$-matrix exhibits a central symmetry about the origin $y = y' = 0$.

(*d*) Symmetry with respect to the interchange of the probe pair,

$$(y, z) \leftrightarrow (y', z'), \quad S_{\alpha\beta}(y, y', \Delta z, f) = S_{\alpha\beta}^{*}(y', y, -\Delta z, f). \tag{2.15}$$

For $\Delta z = 0$, this property implies that $\mathrm{Re}\{S_{\alpha\alpha}\}$ is symmetrical about the line $y = y'$, while $\mathrm{Im}\{S_{\alpha\alpha}\}$ is antisymmetric. Combining (2.13) and (2.15), one can show that diagonal terms of the S-matrix are Hermitian, that is, $S_{\alpha\alpha}(y, y', \Delta z, f) = S_{\alpha\alpha}^{*}(y', y, \Delta z, f)$.

The last two properties are useful as a check on the accuracy of the cross-spectral measurements in the (y, z)-plane.

A discrete windowed Fourier transform, Bendat & Piersol (1986) of the digitized time-series velocity fluctuation data was used to compute (2.5),

$$\hat{u}_{\alpha}(y, z; n\Delta f) = \Delta t (\tfrac{8}{3})^{1/2} \sum_{k=0}^{N_p-1} w(k, N_p) u_{\alpha}(y, z; k\Delta t) \exp(-2\pi \mathrm{i} k n / N_p), \tag{2.16}$$

$$n = 0 \dots N_p - 1,$$

where Δt is the sampling interval, $\Delta f = 1/T = f_s/N_p$, f_s is the sampling frequency, $N_p = 2^p$ is the number of points per data block, with $p = 10$, T is the data block time duration and $w(k, N_p)$ is a suitably chosen windowing function to suppress side lobe spectral leakage. A number of windowing functions were tried early on with the

best results obtained with the Hanning window, Bendat & Piersol (1986),

$$w(j, N) = 1 - \cos^2(j\pi/N), \qquad j = 0 \ldots N - 1, \qquad (2.17)$$

which was selected for use in this study. The factor $(\frac{8}{3})^{1/2}$ appearing in (2.16) properly accounts for the signal content lost in the windowing process. In order to compute $\Phi_{\alpha\beta}(y, y'; f, k_z)$ via (2.6), the S-matrix was extended to negative Δz by application of (2.13) and a discrete *spatial* Fourier transform was performed with a Hanning weighting function (2.17) to obtain

$$\Phi_{\alpha\beta}(y, y'; n\Delta f, m\Delta k_z)$$

$$= \Delta z (\tfrac{8}{3})^{1/2} \sum_{k=-N_z}^{N_z} w(k, N_e)\{\pm S_{\alpha\beta}(y, y', kh, n\Delta f)\} \exp(-ikm/N_e),$$

$$m = 0 \ldots (N_e - 1), \qquad (2.18)$$

where $N_e = 2N_z + 1$, N_z is the number of z measurement locations at a fixed streamwise location, h is the spatial step size between consecutive z-locations, $\Delta k_z = 2\pi/(N_e h)$. Again, only the first $(2N_z + 1)/2 = N_z$ points $m = 0 \ldots N_z - 1$ are given unambiguously. A fast Fourier transform algorithm was used to compute both (2.16) and (2.18).

2.2.1. *Calculation of the POD eigenmodes*

At a fixed x/D location the $\Phi_{\alpha\beta}$-correlation tensor is known at a finite number of equally spaced lateral positions across the jet $\{y_i\}, i = 1, \ldots, m$, where m is the number of X-wire probes in one rake; for the two-rake experiment $m = 8$. Consequently, integrals should be replaced with a finite quadrature form. Details of the numerical integration procedure are presented in Gordeyev (1999). The finite approximation of the integration (2.7) for $3m$-vector $\boldsymbol{\phi} = (\boldsymbol{\phi}_u, \boldsymbol{\phi}_v, \boldsymbol{\phi}_w)^T$, $\boldsymbol{\phi}_\alpha = \{\phi_\alpha(y_i; f, k_z)\}_{i=1}^m$ can be written in the following form:

$$\sum_{j=1}^m \Phi_{\alpha\beta}(y_i, y_j; f, k_z) w(y_j) \phi_\beta^{(n)}(y_j; f, k_z) \Delta y = \lambda^{(n)}(f, k_z) \phi_\alpha^{(n)}(y_i; f, k_z), \qquad (2.19)$$

or

$$\Phi_{\alpha\beta} \boldsymbol{W} \boldsymbol{\phi}_\beta = \frac{\lambda}{\Delta y} \boldsymbol{\phi}_\alpha, \qquad (2.20)$$

where the summation is applied on repeated indices and the $\boldsymbol{W}$-matrix is a *weighting* $[m \times m]$ matrix,

$$\boldsymbol{W} = \overbrace{\{\boldsymbol{w}, \ldots, \boldsymbol{w}\}}^{m-\text{columns}}, \qquad \boldsymbol{w} = \{0.5, \overbrace{1, 1, \ldots, 1}^{m-2}, 0.5\}^T\text{-weighting } m\text{-vector}, \qquad (2.21)$$

$\Phi_{\alpha\beta} = \{\Phi_{\alpha\beta}(y_i, y_j; f, k_z)\}_{i,j=1}^{m,m}$ is the $[m \times m]$ Hermitian matrix and Δy is the spacing between probes in the rake. After multiplication, the $\Phi\boldsymbol{W}$-matrix is no longer a Hermitian matrix. We next multiply (2.19) by $\boldsymbol{W}^{1/2}$ from the left and rearrange to obtain,

$$\boldsymbol{W}^{1/2} \Phi_{\alpha\beta} \boldsymbol{W} \boldsymbol{\phi}_\beta = (\boldsymbol{W}^{1/2} \Phi_{\alpha\beta} \boldsymbol{W}^{1/2})(\boldsymbol{W}^{1/2} \boldsymbol{\phi}_\beta) = \frac{\lambda}{\Delta y} (\boldsymbol{W}^{1/2} \boldsymbol{\phi}_\alpha), \qquad (2.22)$$

or

$$\tilde{\Phi}_{\alpha\beta} \tilde{\boldsymbol{\phi}}_\beta = \frac{\lambda}{\Delta y} \tilde{\boldsymbol{\phi}}_\alpha. \qquad (2.23)$$
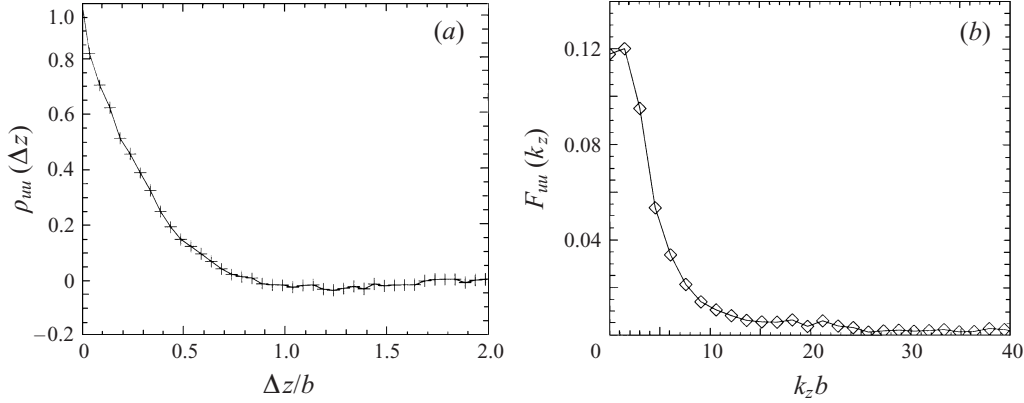
FIGURE 5. (*a*) Sample of *u*-component correlation coefficient $\rho_{uu}(\Delta z)$ and (*b*) its spatial Fourier transform $F_{uu}(k_z)$ at $x/D = 70$. For definition, see equations (2.24) and (2.25).

Now $\tilde{\Phi}_{\alpha\beta} = \mathbf{W}^{1/2}\Phi_{\alpha\beta}\mathbf{W}^{1/2}$ is a Hermitian matrix with $\lambda/\Delta y$, and $\tilde{\phi}_\alpha = \mathbf{W}^{1/2}\phi_\alpha$ being corresponding eigenvalues and eigenvectors, respectively. The matrix equation (2.22) was solved using a Hermitian Matrix Solver in the IMSL library for UNIX systems. After a back transformation $\phi_\alpha = \mathbf{W}^{-1/2}\tilde{\phi}_\alpha$, a finite set of *m* orthogonal spatial modes at the discrete spatial points $\phi_\alpha^{(n)}(y_i; f, k_z)$ with the corresponding eigenvalues $\lambda^{(n)}(f, k_z)$ is obtained.

The number of eigenmodes that can be resolved is limited by the need to avoid spatial aliasing as described by Glauser & George (1992). In this experiment it is found that *m* probes generally allow $m/2$ modes to be resolved although, as described below, this also depends on the particular velocity component considered. Spatial and temporal aliasing issues are addressed in the next section.

2.2.2. *Temporal and spatial aliasing concerns*

The acquired data are discrete in both time and space and therefore careful consideration must be given to avoid temporal and spatial aliasing. Avoidance of aliasing in the homogeneous directions is straightforward and is considered first. More subtle considerations are required in the non-homogeneous direction.

In the two-rake experiment, the traverse system allows one to control the spanwise position of the second rake with respect to the first. At each streamwise location investigated, one rake is placed in the (x, y)-centreplane midway between the flow field confining plates, which corresponds to $z = 0$. The second rake is sequentially positioned below the first rake at $N_z = 15$ different equally spaced z-locations. In order to establish the appropriate z increment for these measurements (which we denote as h), consideration was given to the character of the spanwise correlation coefficient function,

$$\rho_{uu}(\Delta z) \equiv \frac{\overline{u(y, z)u(y, z + \Delta z)}}{\overline{u^2(y, z)}}. \tag{2.24}$$

Figure 5(*a*) presents a sample correlation coefficient function obtained at $x/D = 70$ for 40 equally spaced z-locations with a Δz step size of 4.5 mm. This step provides a maximum resolved wavenumber $k_z^{(\mathrm{max})} = 698\,\mathrm{m}^{-1}$. The *u*-component spanwise macroscale is found to be approximately $\Lambda_z/b = 0.22$. It is noted here that the spanwise macroscale based on the fluctuating *v*-component was somewhat larger, $\Lambda_z/b = 0.35$. This has been observed by other investigators (e.g. Everitt & Robins
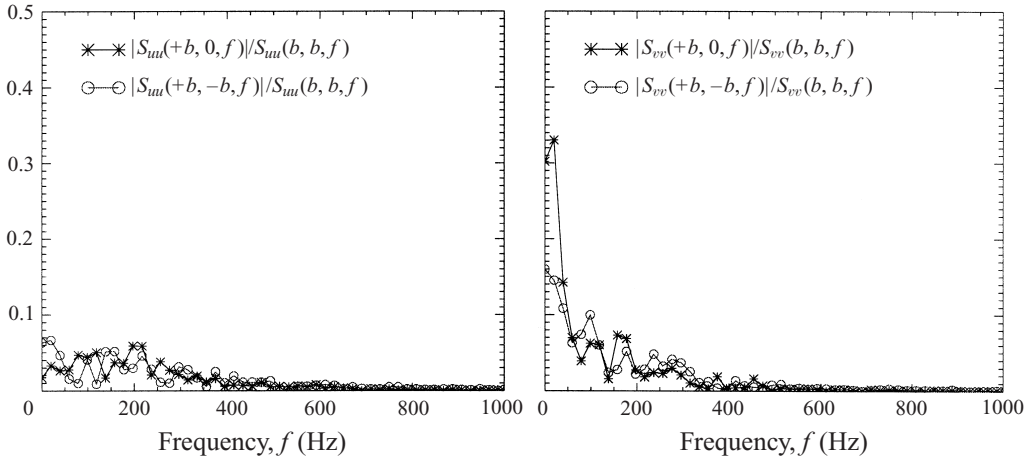
FIGURE 6. Normalized spectral cross-correlations $|S_{uu}(+b, y', f)|/S_{uu}(b, b, f)$ and $|S_{vv}(+b, y', f)|/S_{vv}(b, b, f)$ between two probes for $y' = 0, -b$ at $x/D = 70$.

1978; Antonia *et al.* 1983; Thomas & Brehob 1986). In figure 5(*a*), the probe separation Δz is made non-dimensional with the local mean velocity half-width. A spatial Fourier transform of the correlation coefficient function yields a cross-spectral density function of spanwise wavenumber k_z:

$$F_{uu}(k_z) = \frac{1}{\pi} \int_0^\infty \rho_{uu}(\Delta z) e^{ik_z \Delta z} \, d(\Delta z) \tag{2.25}$$

Figure 5(*b*) presents $F_{uu}(k_z)$ corresponding to the $\rho_{uu}(\Delta z)$ of figure 5(*a*). From this figure (and other similar measurements that are not presented here) one observes that there is little spanwise correlation for $k_z b > 15$. Defining $k_{z \max} \equiv 15/b$ we then require that h satisfy the Nyquist constraint,

$$k_{z \max} \leqslant \frac{\pi}{h}. \tag{2.26}$$

This gives the requirement that $h \leqslant 0.21b$ or equivalently, $h \leqslant \Lambda_z$. The selected value of the stepsize in the z-direction was chosen to be $h = 1.91$ cm for all streamwise stations. This stepsize in z satisfies the Nyquist constraint over the range $50 \leqslant x/D \leqslant 90$. For example, at $x/D = 70$, $h \approx 0.19b$.

For the conditions under which the jet was operated, conventional power spectra obtained in the similarity region reveal that the frequency bandwidth for the fluctuating velocity extends to approximately 5 kHz. In order to avoid temporal aliasing and to satisfactorily characterize the turbulence, this would dictate a sampling frequency for conventional turbulence measurements of approximately 10 kHz. Indeed, this was the sampling frequency used for the measurements shown in figures 3(*a*) and 3(*b*). However, since the focus of this experiment is on the large-scale structure in the flow which is investigated via cross-spectral methods, it will be shown that a much lower sampling frequency combined with the use of analog anti-alias filters offers the best approach. Converged cross-spectral density functions $S_{\alpha\alpha}(y, y'; f)$ obtained with a sampling frequency of $f_s = 10$ kHz at a variety of locations in the jet similarity region show that significant correlation is restricted to much lower frequencies, even for the smallest cross-stream probe spacing. As an example figure 6 presents both $|S_{uu}(+b, y'; f)|/S_{uu}(b, b; f)$ and $|S_{vv}(+b, y'; f)|/S_{vv}(b, b; f)$ as obtained for $y' = 0$,

$-b$ at $x/D = 70$. Note that there is virtually no spectral coherence for frequencies $f > 400\,\text{Hz}$. From this figure (and others that are not presented here) it can be seen that the spatially coherent structures in the similarity region of the jet lie at comparatively low frequencies, so the use of relatively low sampling rates is justified for two-point correlation measurements. In general, it is found that the cross-spectral functions exhibit little correlation for local non-dimensional frequencies $fb/U_M > 1$. Consequently, the local non-dimensional sampling frequency for the experiments was set at $f_s b/U_M = 8.0$. Using (2.1) and (2.2), this gives a streamwise variation of the sampling frequency as $f_s(x/D) = 170\,U_0/D(x/D)^{-3/2} = 4.7 \times 10^5 (x/D)^{-3/2}$ (Hz). For the range of x/D investigated in this experiment the sampling frequency varied from $1.3\,\text{kHz}$ at $x/D = 50$ to $0.55\,\text{kHz}$ at $x/D = 90$. In each case the cutoff frequency of the anti-alias analog filters was set to $f_s/2$ in order to prevent temporal aliasing.

In order to ensure stationary statistics, convergence tests were performed. For the sampling rates quoted above, these showed that by sampling the fluctuating velocity in blocks of $N_p = 1024$ points for a total of $N_b = 500$ blocks the required cross-spectral statistics were fully converged. This corresponds to a total sample time of between 6.5 and 15.5 minutes as x/D varies from 50 to 90, respectively.

The two-rake experiment uses 8 X-wire probes (per rake), equally spaced in the inhomogeneous y-direction with $\Delta y = 5\,\text{cm}$. In order to assess and minimize the degree of spatial aliasing in the y-direction, use was made of a single-rake experiment with 16 equally spaced X-wires across the jet. Thus the spacing between probes was half that for the two-rake case, $\Delta y_1 = \Delta y/2 = 2.5\,\text{cm}$. In order for the two-rake experiment to correctly resolve the cross-spectral matrix in the y-direction, the spatial Nyquist wavenumber $k_{yN} = \pi/\Delta y$ must be greater than the maximum wavenumber exhibiting non-zero lateral spatial correlation. At each x/D location the cross-spectral density $S_{\alpha\alpha}(y, y', St)$ (where $St = fb/U_M$) was computed between all probe pairs. For the 16-probe rake this represents a total of 120 cross-spectral measurements at each streamwise location for each combination of velocity components S_{uu}, S_{vv} and S_{ww}. A spatial Fourier transform of the resulting cross-spectra yields

$$X_{\alpha\alpha}(k_y, y, St) = \int S_{\alpha\alpha}(y', y, St)e^{-ik_y y'}\,\text{d}y'. \qquad (2.27)$$

Of particular interest is the magnitude $|X_{uu}(k_y, y, St)|^2$, which is plotted as a function of $k_y b$ for selected representative values of the parameter St in figure 7. Similar results were examined for $|X_{vv}(k_y, y, St)|^2$ and $|X_{ww}(k_y, y, St)|^2$. Figure 7 shows that all significant lateral correlation of streamwise fluctuations occurs for $k_y b \leqslant 4.4$. Similar results based on the magnitude of $X_{vv}(k_y, y, St)$ and $X_{ww}(k_y, y, St)$ show significant spectral content limited to $k_y b \leqslant 3.2$ and 6.2, respectively. In order to avoid spatial aliasing in the measurement of $S_{uu}(y', y, St)$ it is required that the lateral probe spacing $\Delta y/b \leqslant 2\pi/(2k_y b)_{\text{max}} = 0.7$. This corresponds to a requirement on lateral probe spacing of between $4.44\,\text{cm}$ at $x/D = 50$ to $8\,\text{cm}$ at $x/D = 90$. The requirements for measurement of $S_{vv}(y', y, St)$ are less stringent. In this case the required lateral probe separation varies from $6.4\,\text{cm}$ to $11.4\,\text{cm}$ over the same streamwise range. The most stringent requirement for the avoidance of aliasing is associated with measurement of $S_{ww}(y', y, St)$ which requires a probe separation of from $2.7\,\text{cm}$ to $4.8\,\text{cm}$ over the range $50 \leqslant x/D \leqslant 90$.

Based upon the single-rake measurements, spatial aliasing would not be expected to significantly influence the u- or v-modes except perhaps at $x/D = 50$ where higher-order u modes could be affected. The constraint on the w-component means that only the lowest-order w modes can be faithfully captured. Fortunately, it will be shown
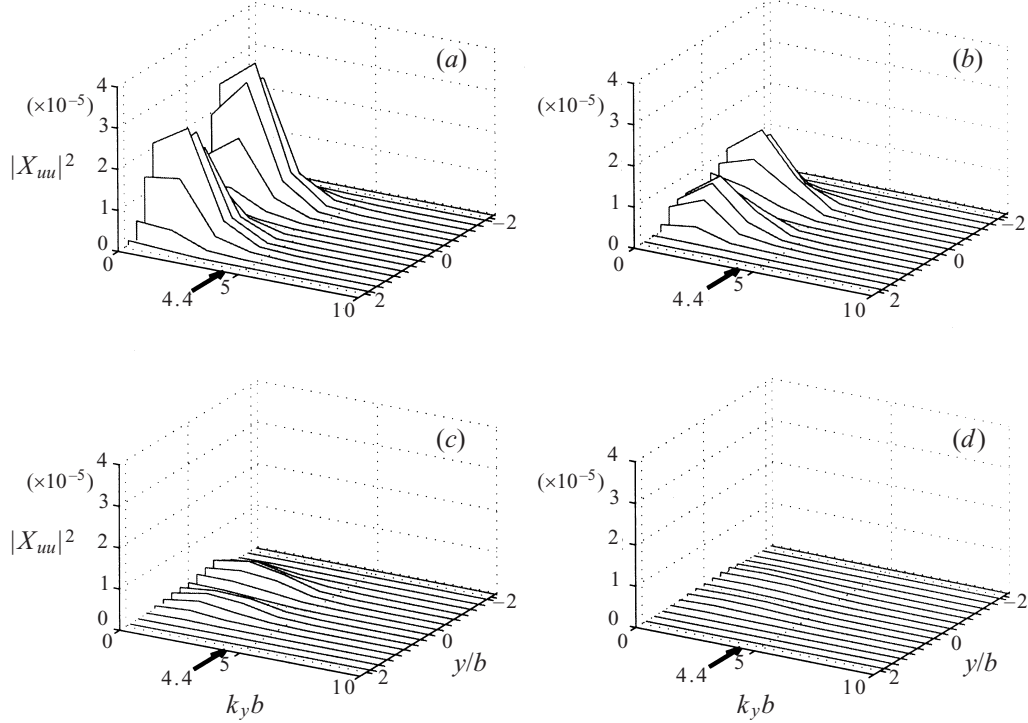
FIGURE 7. $|X_{uu}|^2(y, k_z, St)$ for (a) $St = 0.042$, (b) 0.9, (c) 0.14, (d) 0.18 at $x/D = 70$. For definition of X, see equation (2.27).

that the higher-order w modes are of very low energy so this was not deemed a critical factor in the experiment.

2.3. *Description of the single-rake experiment*

The cross-spectral matrix $S_{\alpha\beta}(y, y', f, \Delta z = 0)$ obtained with the single rake of 16 X-wire probes can be used to compute a set of single-rake POD eigenmodes $\psi_\alpha^{(n)}(y; f)$ with corresponding eigenvalues $\mu^{(n)}(f)$ from the relation

$$\int S_{\alpha\beta}(y, y'; f, \Delta z = 0)\psi_\beta^{(n)}(y'; f)\, dy' = \mu^{(n)}(f)\psi_\alpha^{(n)}(y; f). \tag{2.28}$$

The approach taken in the numerical solution of the above integral equation is similar to that described for (2.7) in §2.2.1. In this case, however, the resulting eigenfunctions are not functions of spanwise wavenumber k_z but depend only on Strouhal number, St, and the inhomogeneous spatial coordinate y. Since the probe spacing in y is one-half that for the two-rake experiment, the spatial resolution of the eigenmodes is improved. However, since the one-rake experiment does not resolve the spanwise direction, the resulting POD modes will represent a weighted sum of the two-rake spanwise-wavenumber-dependent POD modes. Hence, comparison of the results obtained in the one- and two-rake experiments allows one to gauge the effects of rake resolution (because of the larger number of probes in the inhomogeneous coordinate) and the effects of aliasing multiple spanwise wavenumber k_z modes in measurements confined to a single (x, y)-plane.

3. Experimental results

In this section results from both the dual- and single-rake experiments are presented. Before examining the POD eigenfunctions and eigenvalues which form the primary focus of this paper, we give consideration to the form exhibited by the measured cross-spectral matrices, $S_{\alpha\beta}(y, y', St, \Delta z = 0)$ as obtained in the single-rake experiment and $\Phi_{\alpha\beta}(y, y', St, k_z)$ from the dual-rake experiment. As shown by (2.28) and (2.7), these quantities provide the required experimental input for implementation of the POD. In addition, examination of these quantities provides a bridge to earlier studies of the planar jet which have typically utilized correlation methods to infer global structure.

Note that the $S_{\alpha\beta}, \Phi_{\alpha\beta}$ and the derived POD eigenvalues and eigenmodes obtained in the similarity region of the jet form an extensive data set and space limitations allow only a representative sample to be presented here. For those readers interested in examining the full data sets, they may be acquired from either the authors or the JFM editorial office.

3.1. *Character of the cross-spectral matrix* $S_{\alpha\beta}(y, y', St, \Delta z = 0)$

Since many previous studies of coherent structure in the planar jet similarity region have employed two-point correlation measurements obtained in either the (x, y)- or (y, t)-(equivalent to y, f) planes, it seems appropriate to first summarize the characteristics exhibited by the cross-spectral matrix, $S_{\alpha\beta}(y, y', St, \Delta z = 0)$, as measured in the 16-X-wire single-rake experiment. Examination of this spectral matrix reveals similarities between the time-averaged structural patterns exhibited in the planar jet studied here and those investigated in previously cited references. Later, we will also contrast the spatial POD modes extracted in the one- and two-rake experiments. This will demonstrate the unavoidable aliasing of multiple spanwise wavenumber modes that is inherent whenever measurements are confined to a single plane, normal to the z-direction.

Using the single rake, the quantities S_{uu}, S_{vv}, S_{ww}, S_{uv}, and S_{uw} were measured at the five streamwise stations, $x/D = 50, 60, 70, 80$ and 90. In this section selected results are presented only for $x/D = 70$ and these may be considered representative of the other streamwise locations. $S_{\alpha\beta}$ is a complex quantity which depends on the lateral probe positions y and y' as well as temporal frequency, f. In order to present this quantity graphically, we choose to present iso-contours of $\mathrm{Re}\{S_{\alpha\beta}\}$ and $\mathrm{Im}\{S_{\alpha\beta}\}$ in y, y' space for selected representative frequencies f. In presenting these results, the cross-stream coordinate is scaled by the local mean velocity half-width $b(x)$ and the frequency f is scaled by U_M/b to form the local Strouhal number, $St = fb/U_M$. In this representation, the first and third quadrants correspond to probe pairs positioned on the same side of the jet while the second and fourth quadrants represent probes positioned on opposite sides of the jet centreline. Note also that the scalar separation between the two probes increases most rapidly in both directions normal to the line $y = y'$.

Figure 8 presents iso-contours of $\mathrm{Re}\{S_{uu}(y, y', St) \times 10^3\}$ for four representative Strouhal numbers, $St = 0.05, 0.1, 0.14$, and 0.19. Note that the iso-contours of $\mathrm{Re}\{S_{uu}\}$ exhibit a symmetry about the line $y = y'$ and a central symmetry about the origin. The symmetry with respect to the line $y = y'$ is equivalent to symmetry with respect to interchange of the probe positions (2.15). The central symmetry about the origin (2.14) is equivalent to a reflection symmetry with respect to the jet centreplane. Figure 8 shows that positive correlation between streamwise velocity fluctuations occurs only when the two participating probes are located on the same side of the jet centreline
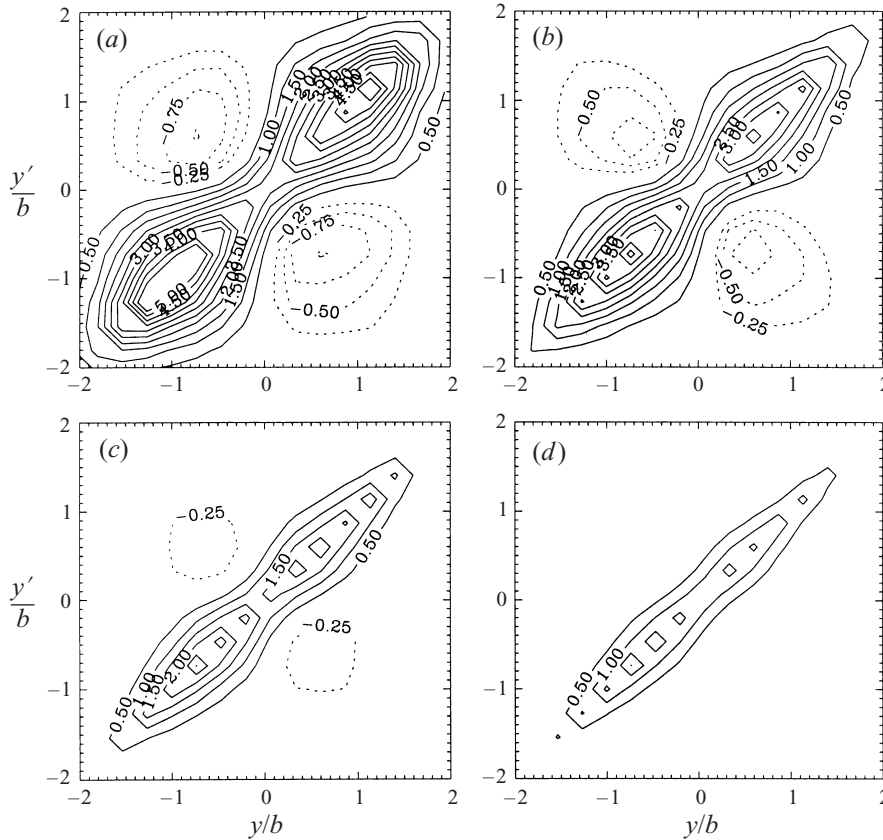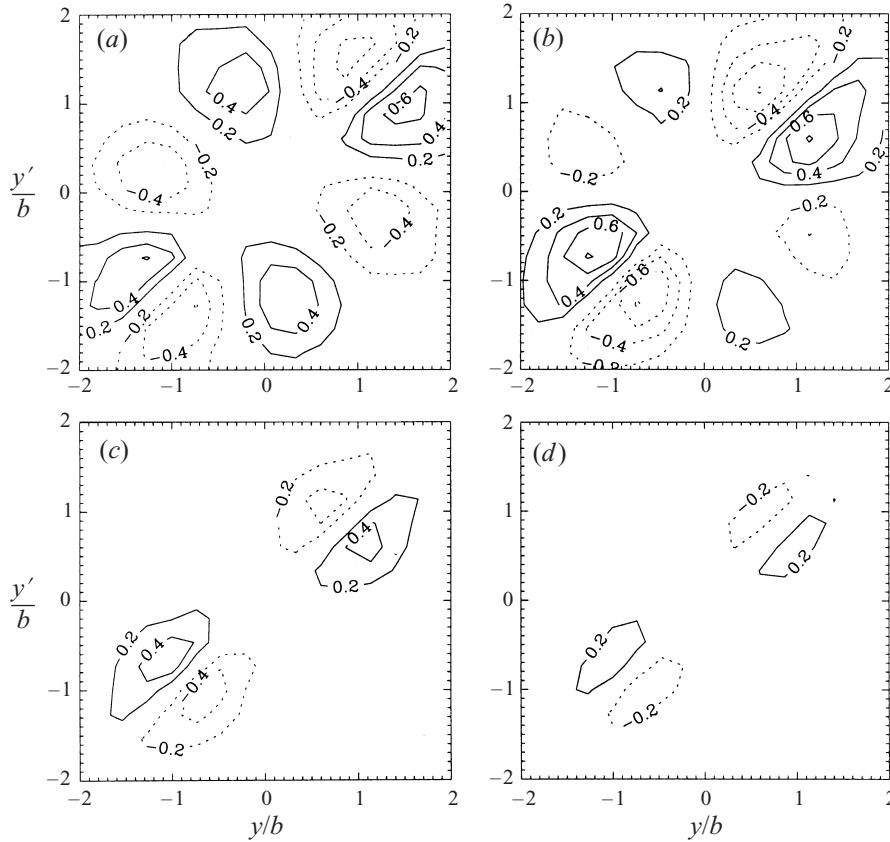
FIGURE 8. The real part of the spectral correlation matrix Re $[S_{uu}(y, y', St)] \times 10^3$ for (a) $St = 0.05$, (b) 0.1, (c) 0.14, (d) 0.19 at $x/D = 70$.

(i.e. y and y' values corresponding to quadrants 1 and 3). In contrast, lobes of negative Re $\{S_{uu}\}$ are apparent in figure 8 for quadrants 2 and 4 which indicates that streamwise fluctuations are negatively correlated on average whenever the probes are positioned on opposite sides of the jet centreline (when y and y' are of opposite sign). That the negative correlation occurs at lower levels is due, in part, to the fact that it is associated with larger probe separations. The existence of negative correlation in figure 8 is a manifestation of the phenomenon that was referred to as 'jet flapping' in the early studies cited in §1.2.

It is the rather striking contour pattern shown in figure 8 that provides strong evidence of the existence an ordered underlying large-scale structure in the planar jet similarity region. The essential character of this pattern is observed to be similar for each of the Strouhal numbers presented in figure 8, the main difference being a reduction in the magnitude of Re $\{S_{uu}\}$ with increasing St. The maximum positive correlation occurs at $y/b = y'/b = \pm 0.9$ for $St = 0.05$ and quickly decays as St increases, with the peak's location gradually shifting to $y/b = y'/b = \pm 0.7$. Note that the level of positive correlation near the jet centreline is much smaller than at off-axis locations. Small positive correlation values near the centre of the jet imply that fine-scale turbulent fluctuations are primarily responsible for the local r.m.s. streamwise fluctuations there. The maximum negative correlation occurs near $(y/b, y'/b) = \pm(0.7, -0.7)$ for $St = 0.05$ which coincides with the location of peak Reynolds stress shown in figure

FIGURE 9. The imaginary part of the spectral correlation matrix Im $[S_{uu}(y, y', St)] \times 10^3$ for (*a*) $St = 0.05$, (*b*) 0.1, (*c*) 0.14, (*d*) 0.19 at $x/D = 70$.

3(*a*). Figure 9 presents iso-contours of Im $\{S_{uu}(y, y', St) \times 10^3\}$. Since this quantity is equivalent to a Fourier sine transform of R_{uu}, interpretation in terms of the physics of the fluctuating velocity field is more difficult. Note, however, that from (2.5), (2.14) and (2.15) Im $\{S_{\alpha\alpha}(y, y, f)\} = $ Im $\{S_{\alpha\alpha}(y, -y, f)\} = 0$, $\alpha = u, v, w$. Examination of figure 9 shows that this gives rise to the eight alternating lobes of positive and negative correlation present. Each of the iso-contour plots in figure 9 is observed to be symmetric with respect to a π rotation about the origin. Note also that the magnitude of Im $\{S_{uu}\}$ is significantly smaller than Re $\{S_{uu}\}$ at corresponding Strouhal numbers.

Figure 10 presents iso-contours of Re $\{S_{vv}(y, y', St) \times 10^3\}$ for the same representative Strouhal numbers as in figures 8 and 9. The observed iso-contour pattern is quite different from that observed in figure 8 with only positive values of Re $\{S_{vv}\}$ present. In particular, figure 10 shows that the lateral fluctuating component exhibits plateau of positive correlation that extend well across the jet centreline. That is, unlike the *u*-component, the fluctuating *v*-component is positively correlated across the jet. In addition, the maximum values of Re $\{S_{vv}(y, y', St)\}$ occur at a Strouhal number of approximately $St = 0.1$. This is consistent with *v*-based spectral and two-point correlation measurements presented in Cervantes & Goldschmidt (1981), Antonia *et al.* (1983), and Thomas & Brehob (1986). Although not presented here, the corresponding iso-contours of Im $\{S_{vv}(y, y', St)\}$ also exhibit maximum values at $St = 0.1$
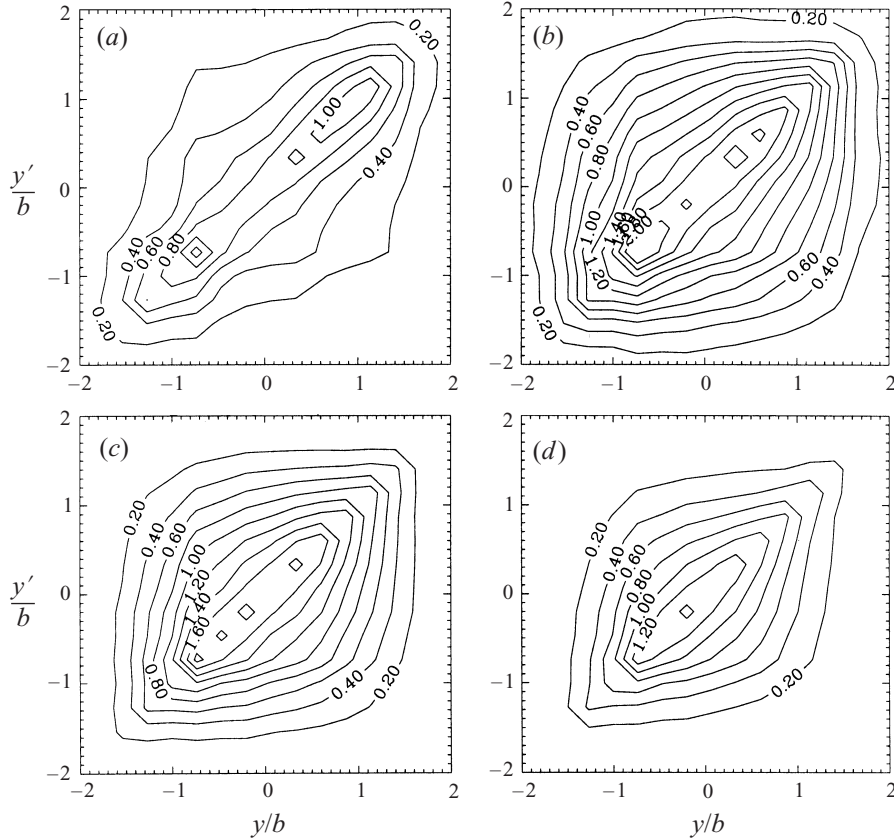
FIGURE 10. The real part of the spectral correlation matrix Re $[S_{uu}(y, y', St)] \times 10^3$ for (a) $St = 0.05$, (b) 0.1, (c) 0.14, (d) 0.19 at $x/D = 70$.

and decay quite rapidly with increasing Strouhal number. As required by symmetry, Im $\{S_{vv}\} = 0$ for $y = y'$ and $y = -y'$. It is also observed that, in general, the values of Im $\{S_{vv}\}$ are substantially smaller than Re $\{S_{vv}\}$, particularly at the higher Strouhal numbers.

Figure 11 presents Re $\{S_{ww}(y, y', St) \times 10^3\}$ iso-contours at the same representative Strouhal numbers as in the previous figures. Small squares visible on the diagonal line $y = y'$ are artifacts of the plotting software. Figure 11 shows that the maximum values of Re $\{S_{ww}\}$ are approximately four times smaller than those for Re $\{S_{uu}\}$. In addition, positive correlation for Re $\{S_{ww}\}$ is restricted to smaller probe seperations as most of the positive contours lie along the diagonal $y = y'$ and these fall off in value rather quickly for $|(y - y')/b| > 0.7$. The peak positive values of Re $\{S_{ww}\}$ are located near $y/b = \pm 0.7$ for $St = 0.14$. Hence peak w-correlation occurs at higher Strouhal numbers than for u or v. Small lobes of negative correlation similar to those observed for Re $\{S_{uu}\}$ are shown in figure 11 at $(y/b, y'/b) = \pm(0.7, -0.7)$. They are most prominent at $St = 0.14$. However, the values are much smaller than those occurring for Re $\{S_{uu}\}$.

Figure 12 presents iso-contours of both the real and imaginary parts of $S_{uv}(y, y', St) \times 10^3$ for the Strouhal number, $St = 0.1$. This Strouhal number exhibits near-peak values of both Re $\{S_{uv}\}$ and Im $\{S_{uv}\}$. Although not presented here, the degree of correlation
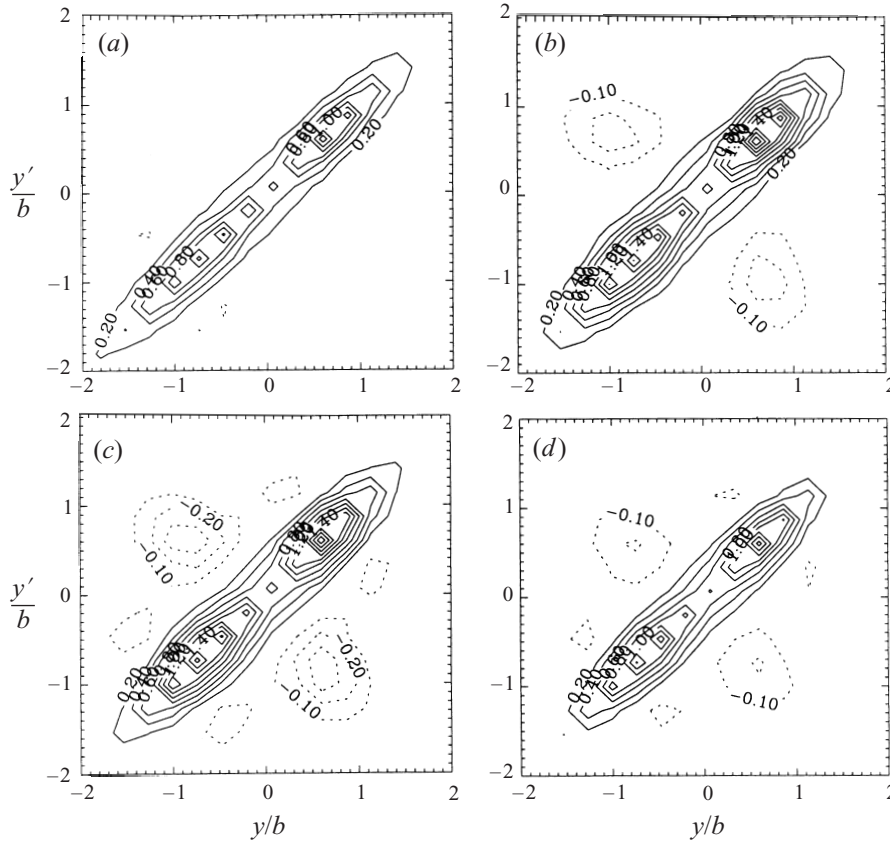
FIGURE 11. The real part of the spectral correlation matrix $\text{Re}\,[S_{ww}(y, y', St)] \times 10^3$ for (a) $St = 0.05$, (b) 0.1 (c) 0.14, (d) 0.19 at $x/D = 70$.

becomes considerably weaker at higher Strouhal numbers. For the measurements presented in figure 12, the u-component is obtained at location y and the v-component at y'. Iso-contours of $\text{Re}\,\{S_{uv}\}$ exhibit positive correlation for $y > 0$ and negative correlation exists for $y < 0$. The maximum value of the correlation magnitude is located near $(y/b, y'/b) = \pm(0.7, 0.7)$ over the range of $St = [0.05\ldots0.1]$. Note that no correlation exists between u- and v-components along the line $y = 0$ (i.e. $\overline{u'(y = 0)v'(y')} = 0$). Recall that the v-component is positively correlated across the jet while the u-component is antisymmetric with respect to the jet centreline. That figure 12 shows that $\text{Re}\,\{S_{uv}\} = 0$ when $y = 0$ but is non-zero for $y' = 0$ indicates that streamwise fluctuations on the centreline must be associated primarily with small scales and are uncorrelated with larger-scale lateral fluctuations. The iso-contours of $\text{Im}\,\{S_{uv}\}$ shown in figure 12 indicate that the imaginary part of the tensor is considerably smaller than the real part.

Although not presented here, three points should be made regarding the real and imaginary parts of $S_{uw}(y, y', St)$. First the magnitude of both the real and imaginary parts of S_{uw} are generally much smaller than for S_{uv} at the same Strouhal numbers. Second, significant values of S_{uw} are restricted to smaller probe separations than for S_{uv}. Finally, the iso-contours exhibit much more complex patterns than for other components of the cross-spectral tensor. These observations, taken together, suggest
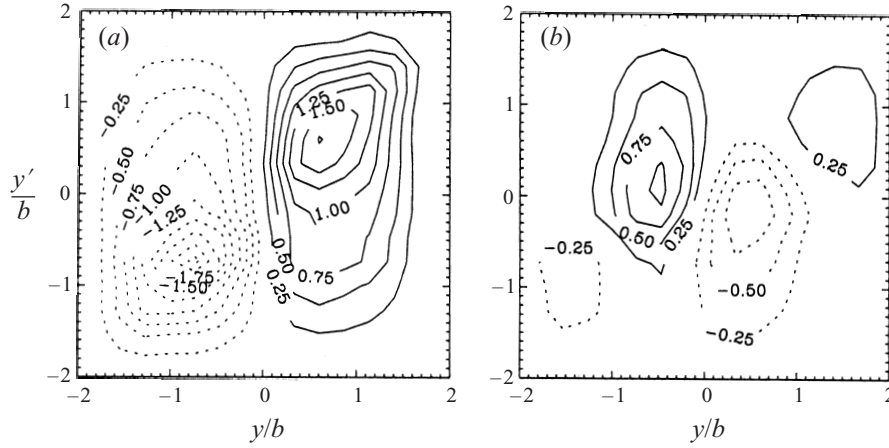
FIGURE 12. (*a*) The real and (*b*) the imaginary parts of the spectral correlation matrix
$S_{uv}(y, y', St) \times 10^3$ for $St = 0.1$ at $x/D = 70$.

that a smaller-scale flow structure is responsible for the $\overline{u'w'}$ correlation than that
responsible for $\overline{u'v'}$.

3.2. *Character of the cross-spectral matrix* $\Phi_{\alpha\beta}(y, y', St, k_z)$

In this section representative results obtained from measurement of the cross-spectral
tensor $\Phi_{\alpha\beta}(y, y', St, k_z)$ in the dual-rake experiment are presented. As shown in (2.6),
$\Phi_{\alpha\beta}$ essentially unfolds $S_{\alpha\beta}$ in spanwise wavenumber space. It also follows from (2.6)
that the determination of the $\Phi_{\alpha\beta}$-matrix requires that the correlation matrix $S_{\alpha\beta}$ be
measured for several different spanwise separations Δz between the two rakes as
described in § 2.

In the presentation of $\Phi_{\alpha\beta}$, the spanwise wavenumber is rendered dimensionless
by the local mean velocity half-width, $b(x)$. As in the previous section, these mea-
surements will be presented in the form of iso-contours of $\Phi_{\alpha\beta}$ in (y, y')-space. In
each case the example presented will correspond to the Strouhal number yielding
peak magnitude of $\Phi_{\alpha\beta}$. The contour plots are presented for selected dimensionless
spanwise wavenumbers, $k_z b$. Although the two-rake measurements were performed
throughout the planar jet similarity region at $x/D = 50, 60, 70, 80$ and 90, only se-
lected measurements at $x/D = 70$ are shown in this section. These may be considered
representative of the other locations.

Figure 13 presents iso-contours of both the real and imaginary parts of $\Phi_{uu}(y, y', St =
0.05, k_z)$ for three selected spanwise wavenumbers. The value $St = 0.05$ corresponds
to the maximum level of Φ_{uu} in the frequency domain. This figure clearly shows
that $\mathrm{Re}\{\Phi_{uu}\}$ and particularly $\mathrm{Im}\{\Phi_{uu}\}$, decay fairly rapidly with increased spanwise
wavenumber. This suggests that the dominant structural component of the flow
responsible for the large-scale streamwise velocity correlation is at least quasi-two-
dimensional. The reader is invited to compare the quantity $\Phi_{uu}(y, y', St = 0.05, k_z = 0)$
as shown here and $S_{uu}(y, y', St = 0.05, \Delta z = 0)$ as shown in figures 8 and 9. The
similarity between the two functions is indicative of the dominance of the planar
$k_z = 0$ mode since

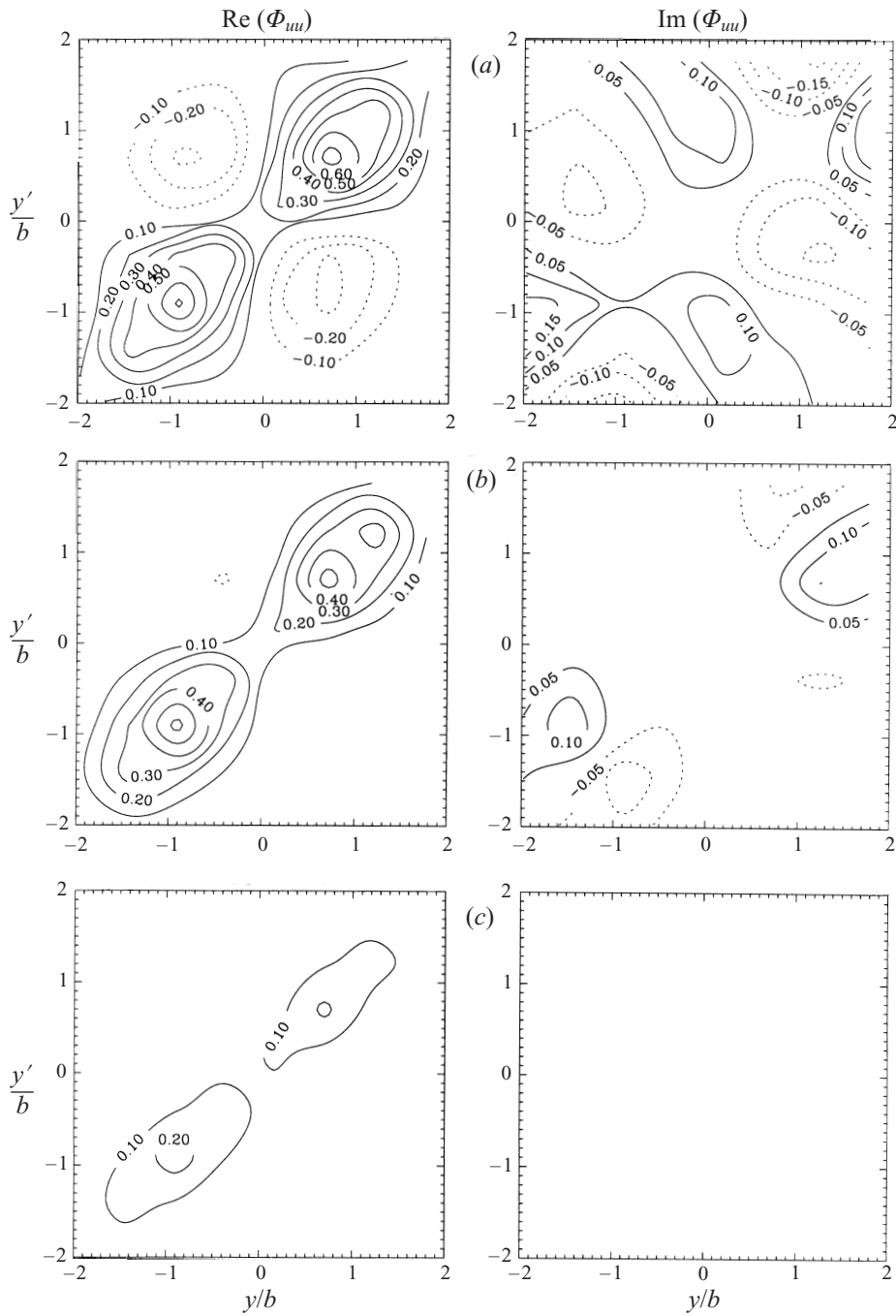$$S_{uu}(y, y', St, \Delta z = 0) = \int \Phi_{uu}(y, y'; St, k_z) \, \mathrm{d}k_z. \tag{3.1}$$

FIGURE 13. The spectral correlation matrix $\Phi_{uu}(y, y', St = 0.05, k_z) \times 10^3$ for
(a) $k_z b/2\pi = 0$, (b) 0.33, (c) 0.66.

In other words, the similarity between these figures indicates that higher-k_z modes must contribute little to S_{uu}. Nevertheless, it must also be noted that some degree of large-scale correlation at non-zero wavenumbers is present in figure 13 and this suggests the presence of a large-spanned three-dimensional structure.
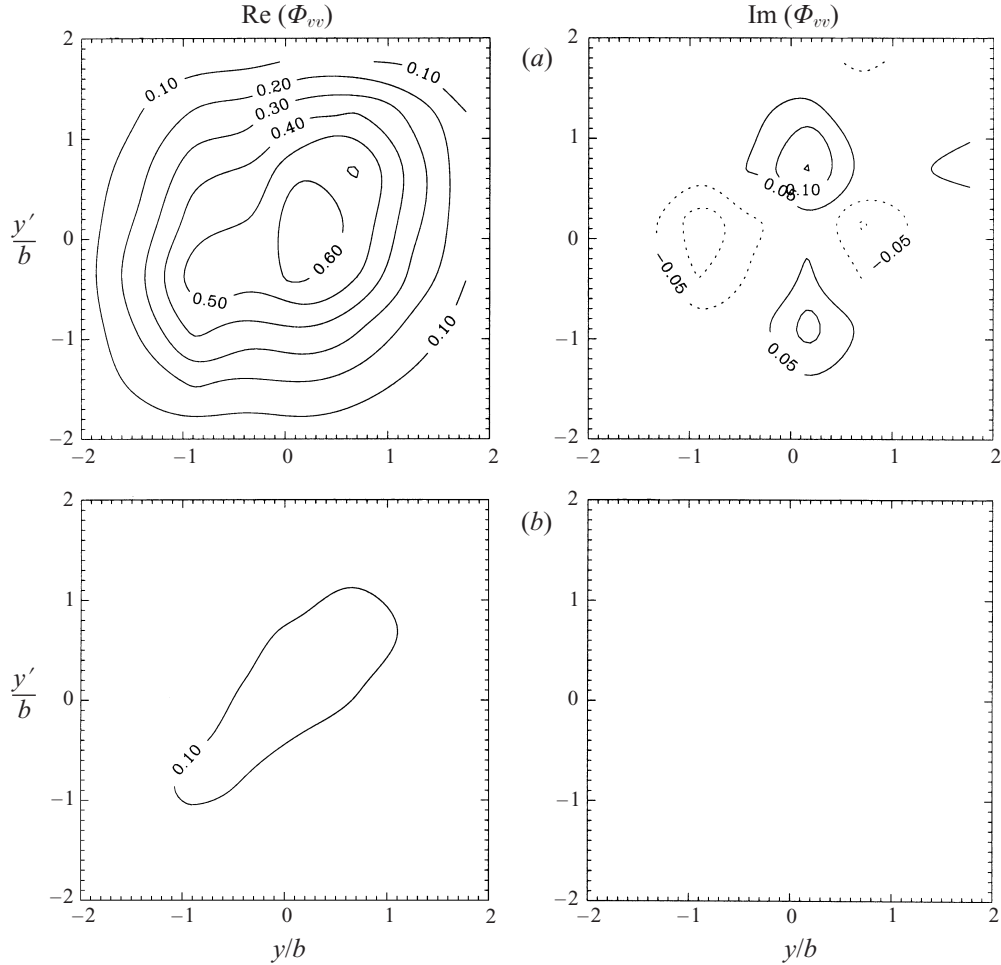
FIGURE 14. The spectral correlation matrix $\Phi_{vv}(y, y', St = 0.1, k_z) \times 10^3$ for (a) $k_z b/2\pi = 0$, (b) 0.33.

Figure 14 presents iso-contours of both the real and imaginary parts of $\Phi_{vv}(y, y', St = 0.1, k_z)$. In this case only two spanwise wavenumbers are shown since the decay of Φ_{vv} with k_z is even more rapid than was the case for the streamwise fluctuations. The implication is that the structure in the flow responsible for the large-scale v-component correlation is quite two-dimensional in nature. This is also apparent upon comparison of Re $[\Phi_{vv}(y, y', St = 0.1, k_z)]$ as shown in figure 14 with Re $[S_{vv}(y, y'; St = 0.1, \Delta z = 0)]$ shown in figure 10. Again, based upon the similarity, one is forced to conclude that higher-wavenumber modes contribute very little to S_{vv}.

The variation of the real and imaginary parts of $\Phi_{ww}(y, y', St = 0.14, k_z)$ with spanwise wavenumber is presented in figure 15. The rate of decay with increased wavenumber is generally smaller in this case suggesting that a non-planar structure is responsible. This is also evident in comparing Φ_{ww} with S_{ww}. Although not shown here, we observe a significant difference, especially in the imaginary parts. This suggests that higher spanwise wavenumber modes are considerably more significant for the w-component fluctuations than was the case for v or u.

Figure 16 presents real and imaginary parts of $\Phi_{uv}(y, y', St = 0.1, k_z)$. This figure
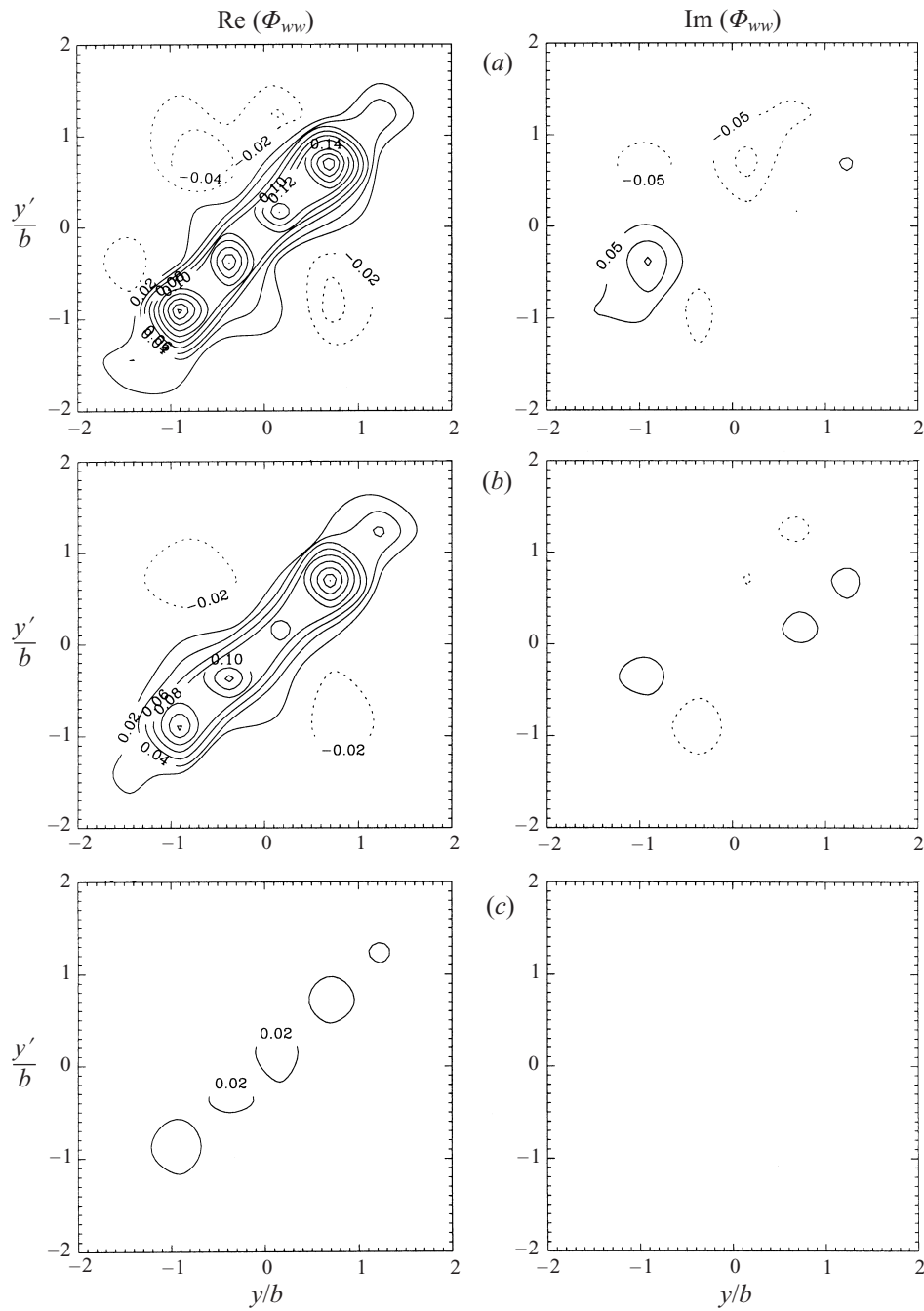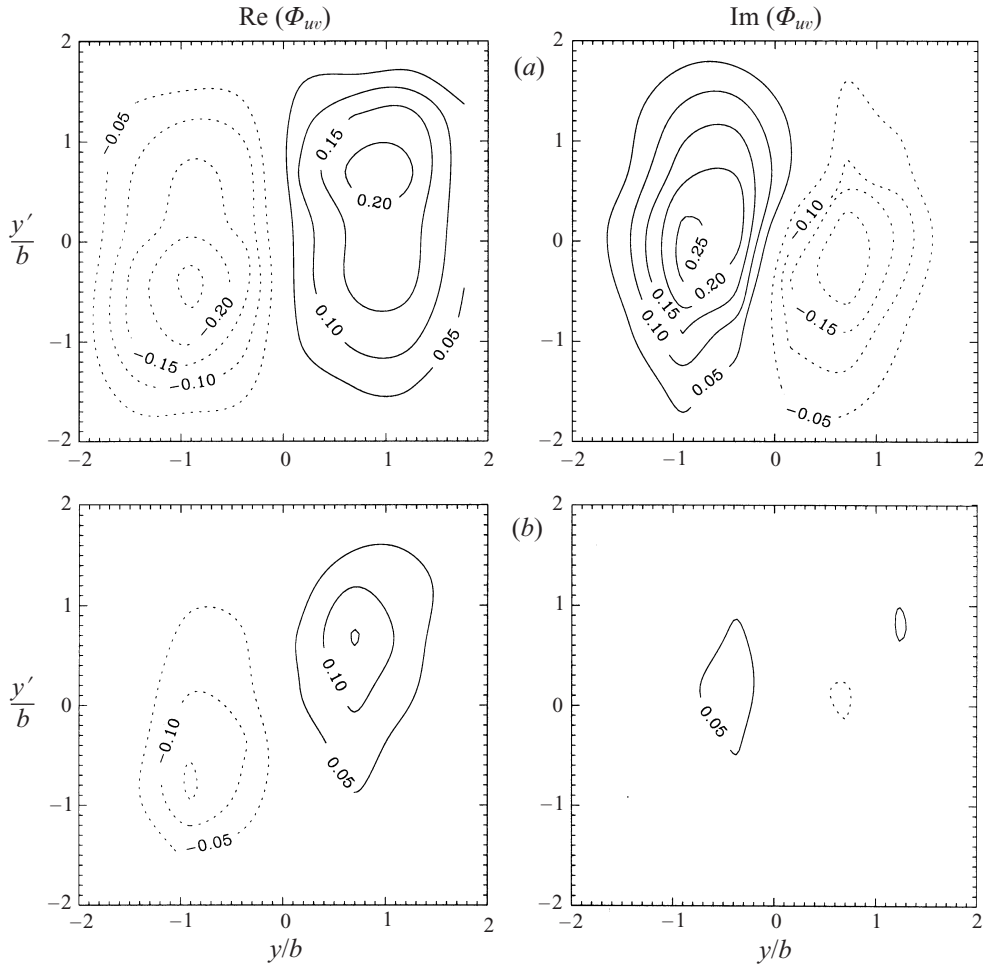
FIGURE 15. The spectral correlation matrix $\Phi_{ww}(y, y', St = 0.14, k_z) \times 10^3$ for
(a) $k_z b/2\pi = 0$, (b) 0.33, (c) 0.66.

reveals a fairly rapid decay of Φ_{uv} with k_z which suggests that motions responsible for
$u'v'$- correlation are largely two-dimensional. This is also apparent from comparison
of figure 16 with S_{uv} as shown in figure 12. The pattern exhibited by Re $\{\Phi_{uv}\}$ is
consistent with the existence of a structure that gives rise to antisymmetric large-

FIGURE 16. The spectral correlation matrix $\Phi_{uv}(y, y', St = 0.1, k_z) \times 10^3$ for (a) $k_z b/2\pi = 0$, (b) 0.33.

scale u-fluctuations and v-fluctuations which exhibit positive correlation across the jet.

In order to clarify the variation of Φ_{uu} with Strouhal number figure 17 presents surface plots of the real part of $\Phi_{uu}(y, y, St; k_z b)$ for four selected wavenumbers $k_z b/2\pi = 0, 0.33, 0.66, 1$. The correlation matrix has two well-defined positive peaks centred near $(y/b = \pm 1, St = 0.05)$. These decay rapidly with increased St, so the spectral correlation for frequencies higher than $St = 0.4$ is completely negligible. Nevertheless, small tails in the correlation at large St suggest some degree of temporal intermittency of the underlying structure. As was observed in figure 13, the maximum values of Re$\{\Phi_{uu}(y, y, St, k_z b)\}$ occur at $k_z = 0$ and become weaker for larger k_z values and virtually no correlation is present for $k_z b > 1$. Note also that at the centreline of the jet correlation values are comparatively small (even for $St = 0.05$ and $k_z = 0$).

The real part of $\Phi_{vv}(y, y', St)$ for $k_z b/2\pi = 0, 0.33, 0.66$ is presented as a surface plot in figure 18. Note that the correlation reaches maximum at $(y = 0, St = 0.1, k_z = 0)$ and quickly decays for larger St and k_z. The levels of Re$\{\Phi_{vv}\}$ shown here are comparable to those shown in figure 17 for Re$\{\Phi_{uu}\}$. Comparison with figure 17
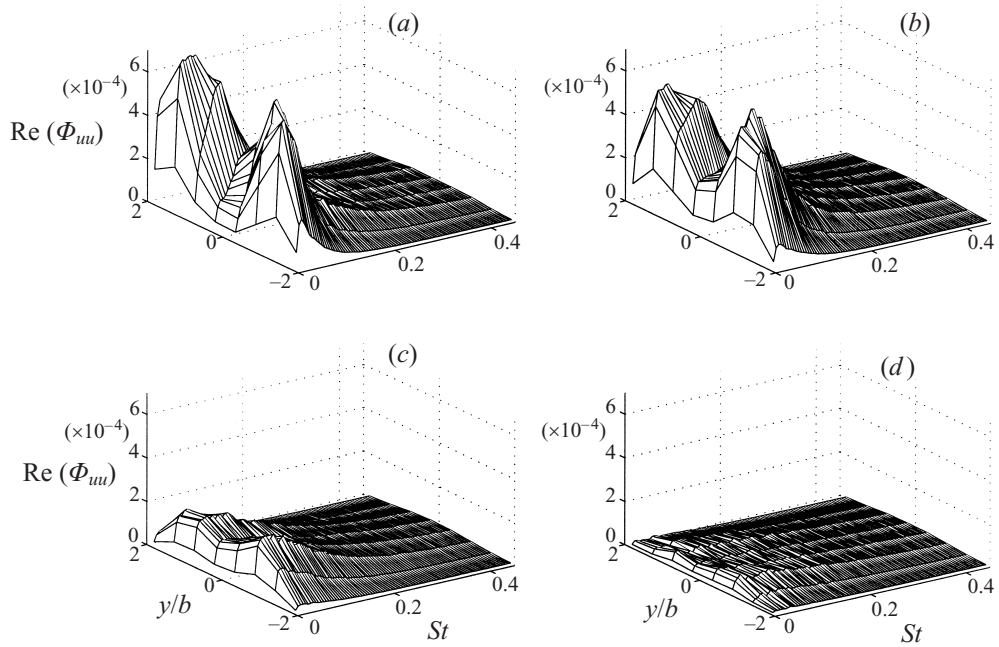
FIGURE 17. The real part of the spectral correlation matrix Re $[\Phi_{uu}(y, y, St, k_z)]$ for (a) $k_z b/2\pi = 0$, (b) 0.33, (c) 0.66, (d) 1.0.
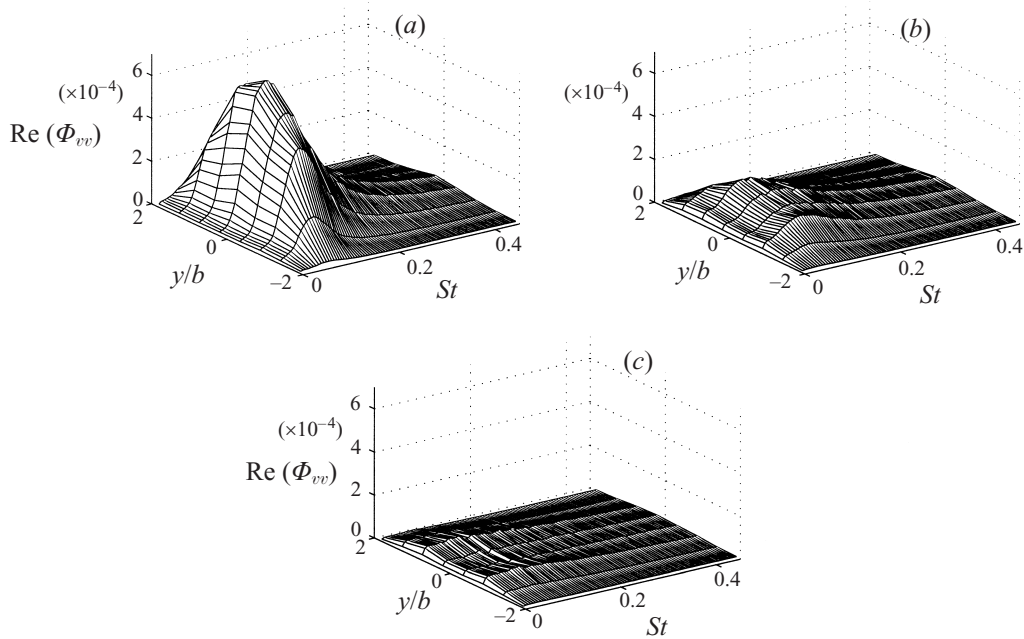

FIGURE 18. The real part of the spectral correlation matrix Re $[\Phi_{vv}(y, y, St, k_z)]$ for (a) $k_z b/2\pi = 0$, (b) 0.33, (c) 0.66.
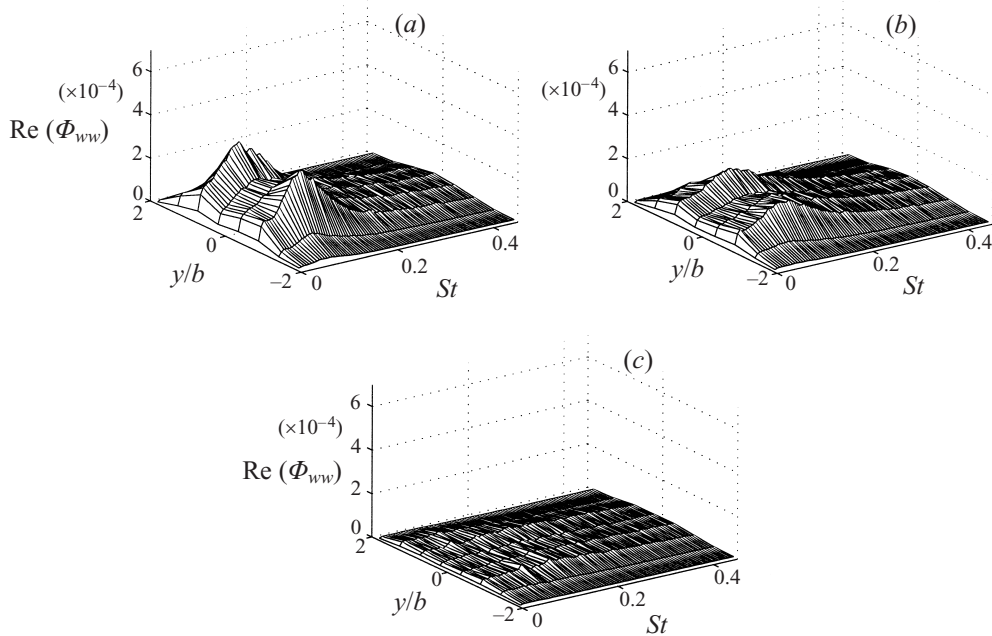
FIGURE 19. The real part of the spectral correlation matrix Re $[\Phi_{ww}(y, y, St, k_z)]$ for (*a*) $k_z b/2\pi = 0$, (*b*) 0.33, (*c*) 0.66.

shows that the decay in k_z is more rapid for Φ_{vv} than for Φ_{uu}. Again low-amplitude tails at larger Strouhal numbers suggest an intermittent underlying structure.

Surface plots of the real part of $\Phi_{ww}(y, y, St)$ for $k_z b = 0, 0.33, 0.66$ are presented in figure 19. The two-positive correlation peaks are located at ($y/b = \pm 0.7$, $St = 0.14$, $k_z = 0$) and no visible correlations exist for $St > 0.4$ or for $k_z b/2\pi > 0.66$ at any St. Comparison with results for Re $\{\Phi_{uu}\}$ and Re $\{\Phi_{vv}\}$ shown in figures 17 and 18, respectively, reveal that the correlation levels associated with the *w*-component are considerably smaller than those for the *u*- and *v*-component fluctuations.

3.3. *POD eigenfunctions and associated eigenvalues obtained from the two-rake experiment*

In this section the POD eigenfunctions and associated eigenvalues obtained from the solution of equation (2.19) using the experimentally obtained cross-spectral matrix $\Phi_{\alpha\beta}$ are presented. Bear in mind that the cross-spectral matrix $\Phi_{\alpha\beta}$ provides a measure of time-averaged large-scale correlation in the flow. Consequently, the extracted POD eigenfunctions are directly related to *an average shape* of the large-scale structure in the jet. Furthermore, both time and the spanwise *z*-direction are transformed into frequency and wavenumber spaces, respectively, by means of Fourier transformations as indicated in (2.5), (2.6). Therefore, the resulting POD eigenfunctions provide the average shape of the structure in a mixed physical–Fourier space (y, St, k_z).

To find the POD modes, the equation (2.7) must be solved. This requires determination of all nine components of the cross-spectral matrix, $\Phi_{\alpha\beta}$. Unfortunately, only the five components Φ_{uu}, Φ_{uv}, Φ_{vv}, Φ_{uw} and Φ_{ww} can be directly measured via the x-wire rakes; the term Φ_{vw} is not directly available. However, as will be described in some detail in §4, this term can be calculated from a knowledge of the other components by means of the continuity equation and by invoking a Taylor's frozen field

approximation. The remaining terms Φ_{vu}, Φ_{wu} and Φ_{vw} follow by using the property that the Φ-matrix is Hermitian.

Our approach to the reconstruction procedure which transforms the POD eigenmodes into the physical domain and allows restoration of the instantaneous shape of the structures, involves a coupling between the continuous wavelet transform, the experimentally determined POD eigenmodes obtained from equation (2.7) and instantaneous realizations of the flow field obtained by means of three spanwise-separated hot-wire rakes. This procedure recovers the phase information necessary for the reconstruction of the physical flow structures and the investigation of their dynamic behaviour. This aspect is the topic of Part 2 and will not be pursued further here. Instead, we focus on the character of the eigenmodes themselves and explore their self-similarity. In order to do this we would like to avoid invoking a Taylor's frozen field approximation which is required to obtain the full $\Phi_{\alpha\beta}$ tensor. Here we will instead present POD modes calculated using only the diagonal terms $\Phi_{\alpha\alpha}$,

$$\int \Phi_{\alpha\alpha}(y, y'; f, k_z)\phi_\alpha^{(n)}(y'; f, k_z)\,\mathrm{d}y' = \lambda_\alpha^{(n)}(f, k_z)\phi_\alpha^{(n)}(y; f, k_z). \qquad (3.2)$$

It is important to note that the above relation excludes any information contained in the off-diagonal terms, Φ_{uv}, Φ_{wv}, and so on. Strictly speaking then, the POD modes derived from solving (3.2) and those obtained from solving (2.7) will be different. In fact, they will be the same only if the off-diagonal terms are zero. Since, as shown in the previous section, Φ_{uu} and Φ_{vv} dominate the off-diagonal term Φ_{uv} we can expect the u- and v- component POD modes obtained by solution of (3.2) to be quite similar to the POD modes obtained by (2.7). In fact, this turns out to be the case as will be shown in Part 2. In the case of the w-mode our results show that Φ_{ww} and Φ_{uw} are of the same order of magnitude. Hence we can expect a more substantial disparity between the w-component POD modes derived from (3.2) and (2.7). Nevertheless, it is also worth mentioning that the set of w-component POD modes obtained via (3.2) is still complete, as follows from (2.9), and can be treated as another completely valid way to investigate the Φ_{ww}-term. Thus, while the u- and v-component POD modes obtained from (3.2) can shed light onto the shape of the structure, more caution must be exercised in forming conclusions regarding the w-component structure based on the presented w-modes. As shown in Part 2, only the w-component POD modes from (2.7), combined with instantaneous phase information obtained from the projection onto the flow field, will provide the physical flow structure responsible for the w-component fluctuation.

In summary, the information contained in the off-diagonal terms of the cross-spectral matrix is crucial for modelling the jet dynamics and for reconstructing the large-scale structure in physical space. The focus of this paper is on (i) the documentation of the cross-spectral matrix, (ii) examination of the basic character of the POD modes in the y, St, k_z domain and (iii) the exploration of the self-similarity of the POD modes and eigenvalues. To do this we exploit the dominance of the diagonal terms in the cross-spectral matrix and thereby avoid use of a Taylor's frozen field approximation by working with (3.2) instead of (2.7).

The POD eigenmodes $\phi_\alpha^{(n)}(y; x/D, St, k_z b)$ with the corresponding eigenvalues $\lambda_\alpha^{(n)}(St, k_z b; x/D)$ were calculated from (2.19) for each individual $\Phi_{\alpha\alpha}$, $\alpha = u, v, w$. We will subsequently refer to $\phi_u^{(n)}$, $\phi_v^{(n)}$ and $\phi_w^{(n)}$ as the nth u-, v- and w-modes, respectively. As was the case in the presentation of the correlation matrices $S_{\alpha\beta}$ and $\Phi_{\alpha\beta}$, we choose to highlight results obtained at $x/D = 70$ and these may be considered
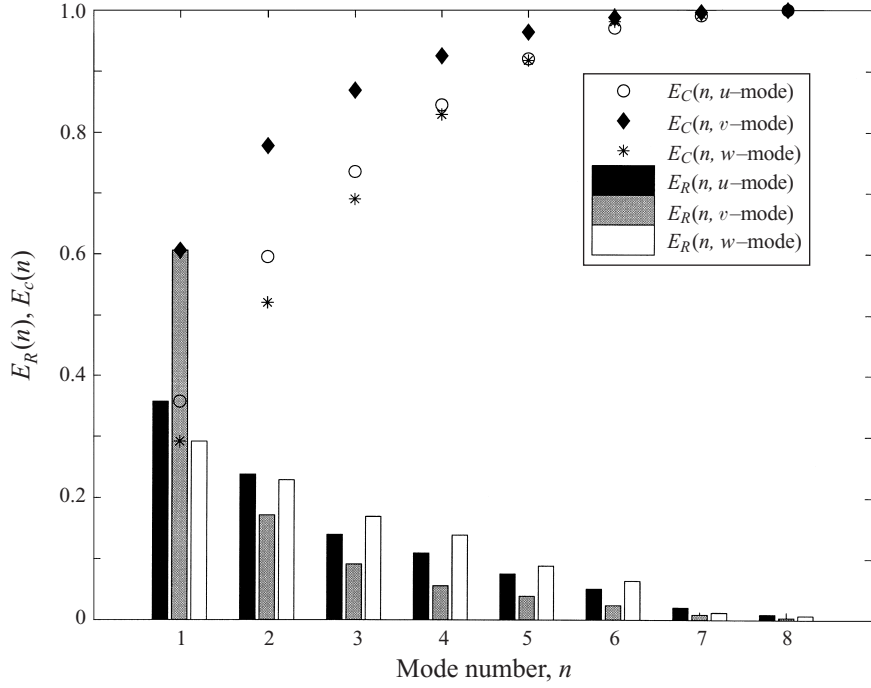
FIGURE 20. Relative $E_R(n, \alpha - \text{mode})$ and cumulative $E_C(n, \alpha - \text{mode})$
energies for u-, v- and w-modes.

representative. Results obtained at the other streamwise locations will be presented when we examine similarity scaling of the eigenfunctions and eigenvalues.

We first give consideration to the energy content of the POD modes as expressed through their respective eigenvalues. For a given fluctuating component α, one can investigate the ratio of energy contained in mode number n to the total energy in large-scale modes resolved by the experiment (see the related discussion in §§ 2.2.2 and 3.2). That is, the relative energy of the α-component mode number n is given by

$$E_R(n; \alpha - \text{mode}) = \frac{\sum_{f,k_z} \lambda_\alpha^{(n)}(f, k_z)}{\sum_n \sum_{f,k_z} \lambda_\alpha^{(n)}(f, k_z)} \tag{3.3}$$

Alternatively, for a given fluctuating component we can consider the cumulative effect of all modes up to the n-th mode again expressed as a ratio of the total energy in that fluctuating component,

$$E_C(n; \alpha - \text{mode}) = \frac{\sum_{k=1}^{n} \sum_{f,k_z} \lambda_\alpha^{(k)}(f, k_z)}{\sum_n \sum_{f,k_z} \lambda_\alpha^{(n)}(f, k_z)} \tag{3.4}$$

Figure 20 presents both $E_R(n; \alpha - \text{mode})$ and $E_C(n; \alpha - \text{mode})$ for the u-, v- and w-components. Note that the first u-mode contains approximately 36% of the total large-scale energy of the u-component and the first four modes account for approximately
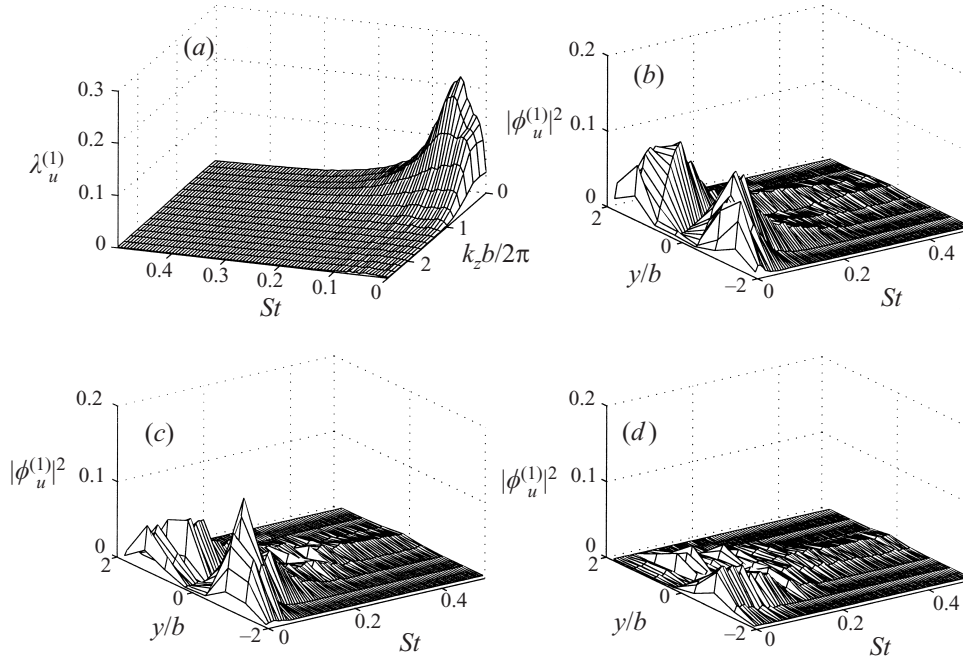
FIGURE 21. The first u-mode: (*a*) Eigenvalues $\lambda_u^{(1)}(f, k_z; x/D = 70)$, and the eigenmodes $|\phi_u^{(1)}(y, St, k_z; x/D = 70)|^2$ for (*b*) $k_z b/2\pi = 0$, (*c*) 0.33 and (*d*) 0.66.

85%. The convergence is even more rapid for the v-component. The first v-mode is responsible for 61% of the large-scale v-component energy with the first three modes capturing nearly 90%. The w-component eigenvalues show a slower convergence, with 33% of the energy contained in the first mode. The first four modes account for over 80% of the w-component energy in the flow. With regard to the possibility of building a low-dimensional model of the self-similar region of the turbulent planar jet, figure 20 is very encouraging. Considering that this is a fully turbulent shear flow, it is of interest to note that such a large fraction of the fluctuation energy is accounted for by the first 3–4 POD modes and this suggests that Galerkin projection of these modes onto the Navier–Stokes equations could provide the basis for a model that can capture the essential large-scale dynamics of the flow (for example, see Aubry *et al.* 1988 and Ukeiley & Glauser 1995).

The eigenvalues $\lambda_u^{(1)}(St, k_z b)$ for the first (and most energetic) u-mode obtained at $x/D = 70$ are presented in figure 21(*a*). The eigenvalues are plotted as a surface in $(St, k_z b)$-space. As such, this figure represents the $\phi_u^{(1)}$ energy distribution in the frequency–spanwise wavenumber domain. The peak u-eigenvalue is located near $(St = 0.05, \; k_z = 0)$. Note that essentially all the energy of the first u-mode is concentrated in a low-wavenumber range $k_z b/2\pi \leqslant 1$. This suggests the existence of a relatively extended modal structure in the spanwise direction (i.e. of order b). Further, the fairly sharp peak in Strouhal number reflects a nearly periodic behaviour in time. There is little energy content for $St > 0.2$.

Because the eigenmodes are orthonormal, examination of equation (2.9) reveals that it is convenient for their presentation to multiply by the corresponding amplitude factor, $(\lambda_\alpha^{(n)}(St, k_z))^{1/2}$. Unless otherwise noted, in the remainder of this paper all POD eigenmodes that are presented have had this amplitude scale factor applied.
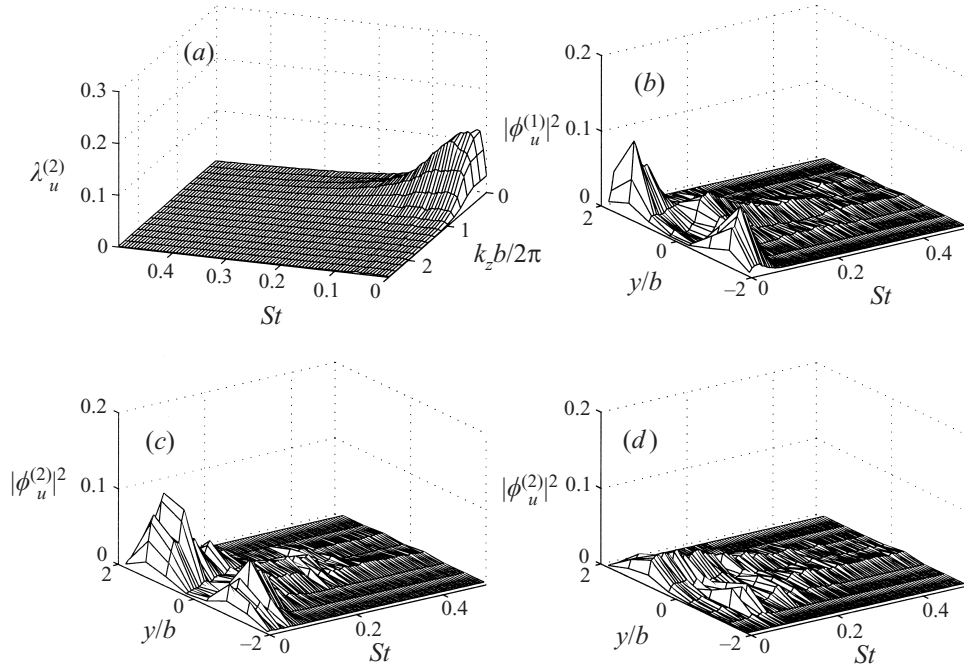
FIGURE 22. The second u-mode: (a) Eigenvalues $\lambda_u^{(2)}(f, k_z; x/D = 70)$, and the eigenmodes $|\phi_u^{(2)}(y, St, k_z; x/D = 70)|^2$ for (b) $k_z b/2\pi = 0$, (c) 0.33 and (d) 0.66.

The modulus-squared of the first u-mode, $\phi_u^{(1)}$, for selected spanwise wavenumbers $k_z b/2\pi = 0, 0.33, 0.66$ is shown in figure 21(b–d). The shape of the u-mode at $k_z = 0$ is symmetric in the y-direction, as evidenced by two symmetrical 'humps' centred near $y/b = \pm 1$. For $k_z b/2\pi = 0.33$ though, figure 21(c) reveals a cross-stream asymmetry whereby the modal amplitude on the $-y$ side of the jet is larger than on the $+y$ side. A similar trend is observed for the case $k_z b/2\pi = 0.66$ shown in figure 21(d). Note however that the modal amplitude is considerably smaller at the larger spanwise wavenumbers.

The second u-mode eigenvalues and eigenfunctions are presented in figure 22. The eigenvalue distribution in (St, k_z)- space is shown in figure 22(a) and exhibits a peak near $(St = 0.03, k_z = 0)$. Note that the peak has a small, relatively flat plateau that extends in the k_z-direction. Again, however, there is little energy content for $k_z b/2\pi > 1$. As was the case for mode 1, the St band of significant energy content is also rather narrow. Figure 22(b) presents the scaled modulus-squared of $\phi_u^{(2)}$ for $k_z = 0$. It is approximately symmetrical in the y-direction. However, higher-wavenumber modes presented in figures 22(c) and 22(d) reflect a cross-stream asymmetry similar to what occurred for u-mode 1. For $k_z b/2\pi = 0.33$ the modal amplitude on the $+y$ side of the jet dominates the $-y$ side. Comparison of this figure with figure 21(c) reveals that the shape of the second mode at $k_z b/2\pi = 0.33$ is almost a mirror image of the first mode at the same wavenumber. The same can be said of a comparison between u-mode 1 and 2 shapes at $k_z b/2\pi = 0.66$ (figures 21d and 22d).

Figure 23(a) presents the eigenvalue distribution in (St, k_z)-space for the first v-mode. Note that the peak energy is associated with $k_z = 0$ and $St = 0.1$. In this case the decrease in energy with increased k_z is much more rapid than for the u-modes previously presented. The first scaled v-mode is shown for selected spanwise
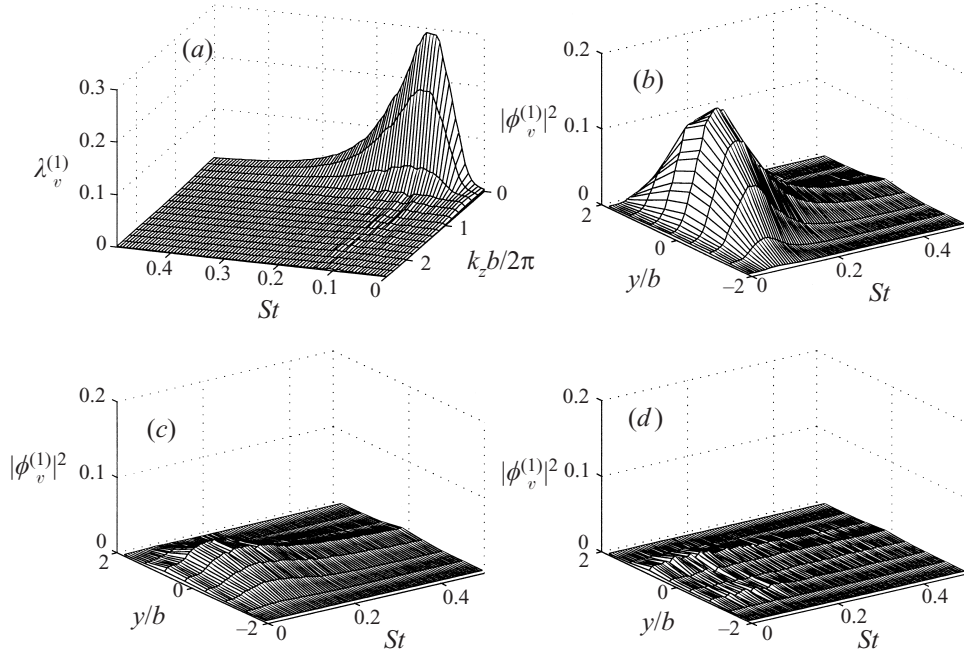
FIGURE 23. The first v-mode: (a) Eigenvalues $\lambda_v^{(1)}(f, k_z; x/D = 70)$, and the eigenmodes $|\phi_v^{(1)}(y, St, k_z; x/D = 70)|^2$ for (b) $k_z b/2\pi = 0$, (c) 0.33 and (d) 0.66.

wavenumbers in figure 23(b–d). The v-mode shows a symmetrical behaviour in the cross-stream direction for $k_z = 0$ with peak amplitude on the jet centreline. For non-zero wavenumbers the shape is similar but the amplitude is greatly reduced. Figure 23 suggests that the first v-mode is essentially planar. Although the second v-mode is not presented here, it exhibits minimum amplitude on the jet centreline and two peaks near $y/b = \pm 1$. The mode shape is similar for both zero and non-zero spanwise wavenumbers. The associated eigenvalue distribution peaks at $k_z = 0$ and $St = 0.10$ but the peak eigenvalue is only about one-sixth the value for v-mode 1. The rapid reduction in $|\phi_v^{(2)}|^2$ with k_z is also indicative of a planar mode.

Finally, a comment should be made about the eigenvalues and squared-modulus of the first w-mode. For the first w-mode, the eigenvalue peak is located at ($St = 0.12$, $k_z = 0$). However, the maximum w-eigenvalue is only one fifth the maximum mode 1 u-eigenvalue. Near $St = 0.12$ the w-mode appears symmetrical in the cross-stream direction for both zero and non-zero wavenumbers. Its shape exhibits a minimum value near the jet centreline and peak values occur near $y/b = \pm 1$. The mode shapes at lower St are asymmetric in y.

3.4. *The self-similarity of the POD modes*

In this section we investigate the self-similarity of the POD eigenvalues and eigen-modes by application of suitable scaling. From (2.3) the dimension of $R_{\alpha\beta}$ is $[L^2 T^{-2}]$, and since $\Phi_{\alpha\beta}$ is a Fourier transform of $R_{\alpha\beta}$ in time t and space z (see equations (2.4) and (2.6)) the appropriate dimension of $\Phi_{\alpha\beta}$ is $[L^2 T^{-2} \cdot L \cdot T] = [L^3 T^{-1}]$. From (2.7) it follows that the appropriate dimension for the eigenvalue λ is $[L^4 T^{-1}]$. Thus, in terms of global flow field variables, the appropriate scaling for λ is $b^3 U_m$ and the
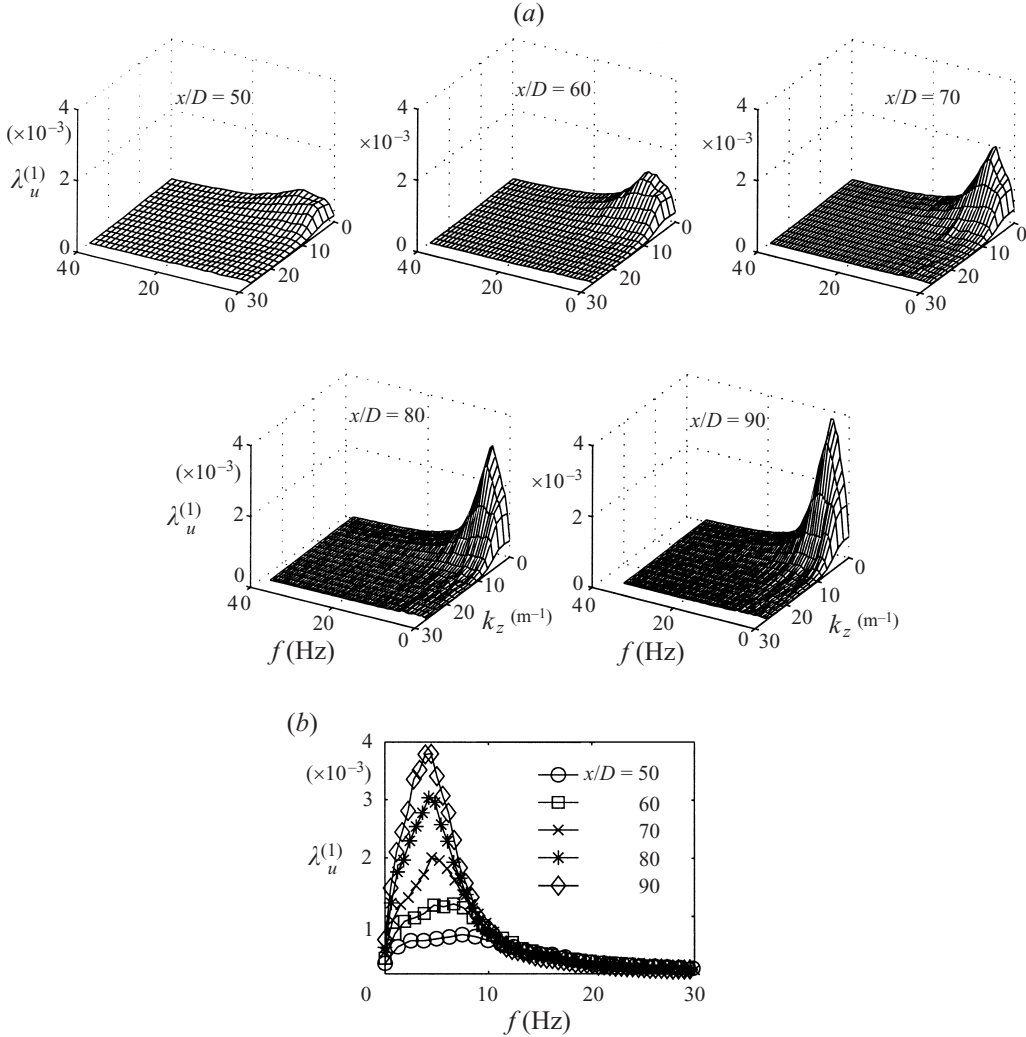
FIGURE 24. (*a*) Unscaled eigenvalues $\lambda_u^{(1)}(f, k_z; x/D)$ for the first *u*-mode for several x/D-stations. (*b*) Streamwise development for $k_z = 0$.

eigenvalues can be written in the following non-dimensional form:

$$\lambda^{(n)}(f, k_z; x/D) = b^3 U_m \tilde{\lambda}^{(n)}(St, k_z b; x/D). \tag{3.5}$$

The appropriate non-dimensionalization for the POD modes will be

$$(\lambda_\alpha^{(n)}(f, k_z; x/D))^{1/2} \phi_\alpha^{(n)}(y; f, k_z, x/D)$$

$$= (b^3 U_m \tilde{\lambda}_\alpha^{(n)}(St, k_z b; x/D))^{1/2} \phi_\alpha^{(n)}(y/b; St, k_z b, x/D). \tag{3.6}$$

An example of the measured eigenvalue variation over the streamwise distance covered in this experiment is presented in figure 24. In particular, figure 24(*a*) shows the streamwise variation of $\lambda_u^{(1)}(f, k_z; x/D)$, the unscaled *u*-component mode 1 eigenvalues over the streamwise range $50 \leqslant x/D \leqslant 90$. This figure shows that the maximum unscaled eigenvalue increases in magnitude and shifts to smaller frequencies with increased streamwise distance. This is also readily apparent from figure 24(*b*) which
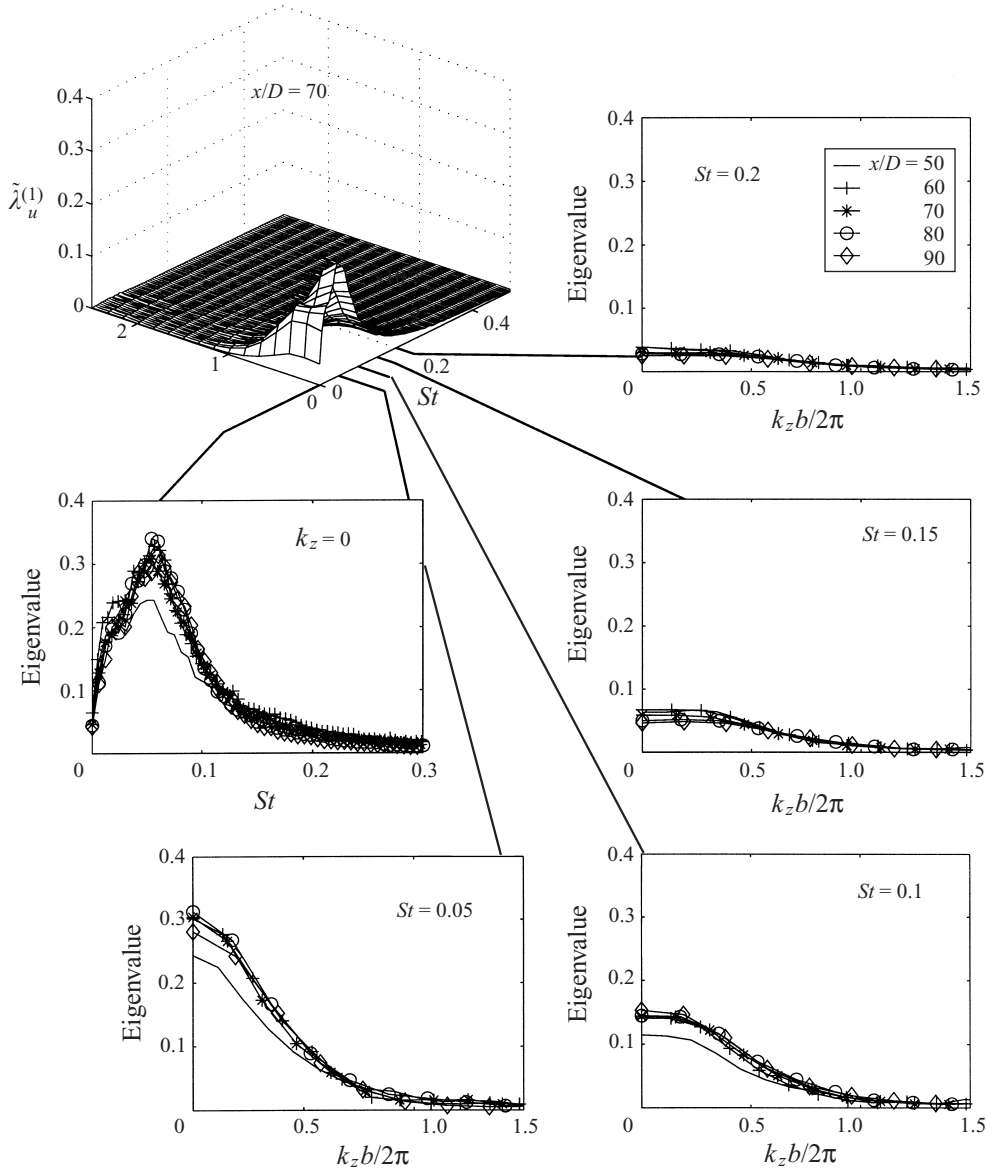
FIGURE 25. Scaled eigenvalues $\tilde{\lambda}_u^{(1)}(St, k_z; x/D)$ for the first u-mode.

highlights the streamwise development of the $k_z = 0$ (i.e. a planar mode) u-component mode 1 eigenvalues.

If the POD eigenmodes and eigenvalues exhibit self-similarity then after a suitable rescaling (3.5) and (3.6), we must have congruence of both the non-dimensional eigenvalues $\tilde{\lambda}_\alpha^{(n)}(St, k_z b; x/D)$ in $(St, k_z b)$-space and the eigenfunctions in $(y/b, St, k_z b)$-space.

Since the eigenvalues form surfaces in St, k_z space this poses a challenge in providing a meaningful comparison at different x/D stations. One way of performing such a comparison is to 'slice' each of the eigenvalue surfaces at selected values of St and compare their variation with spanwise wavenumber k_z and at each streamwise
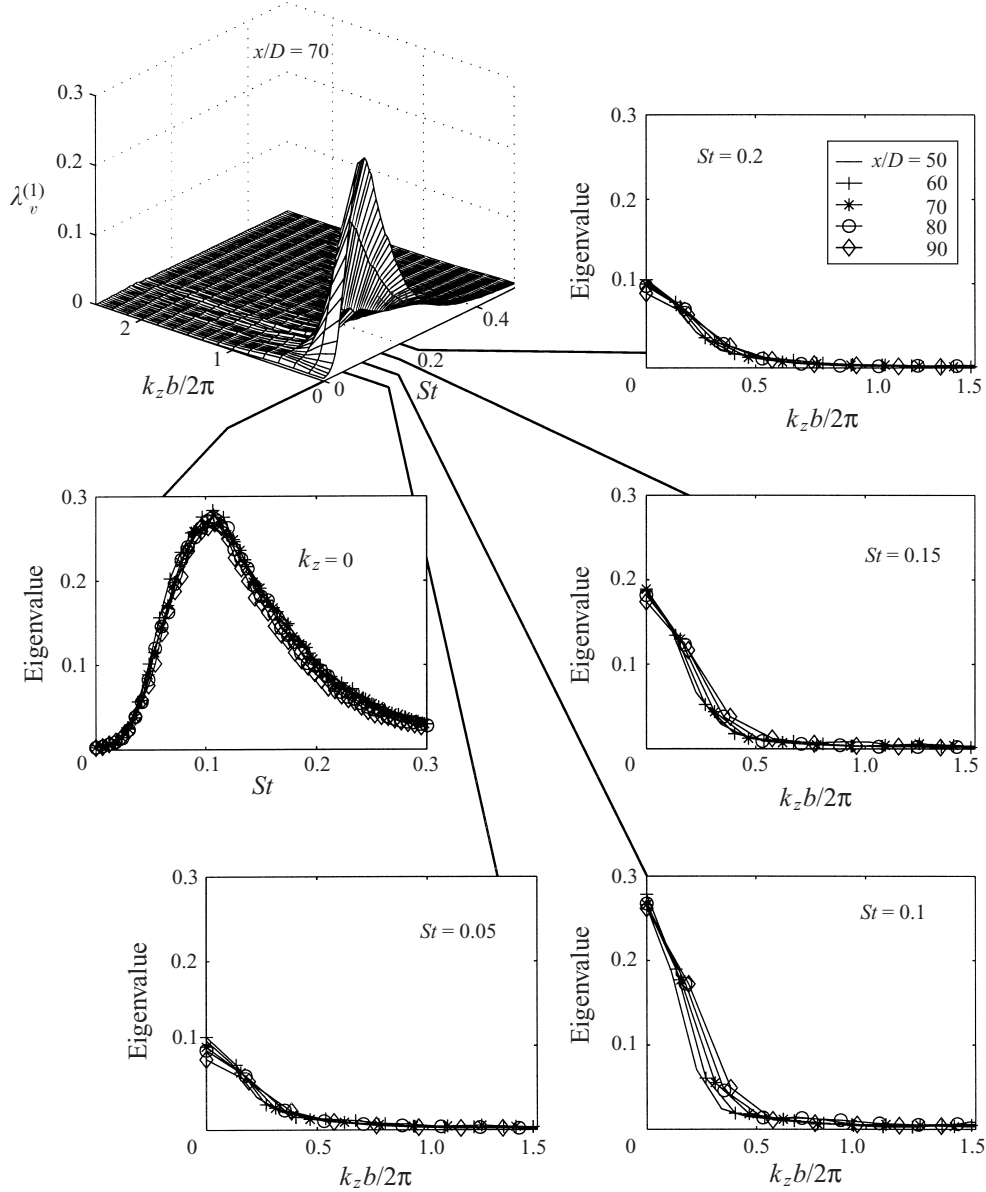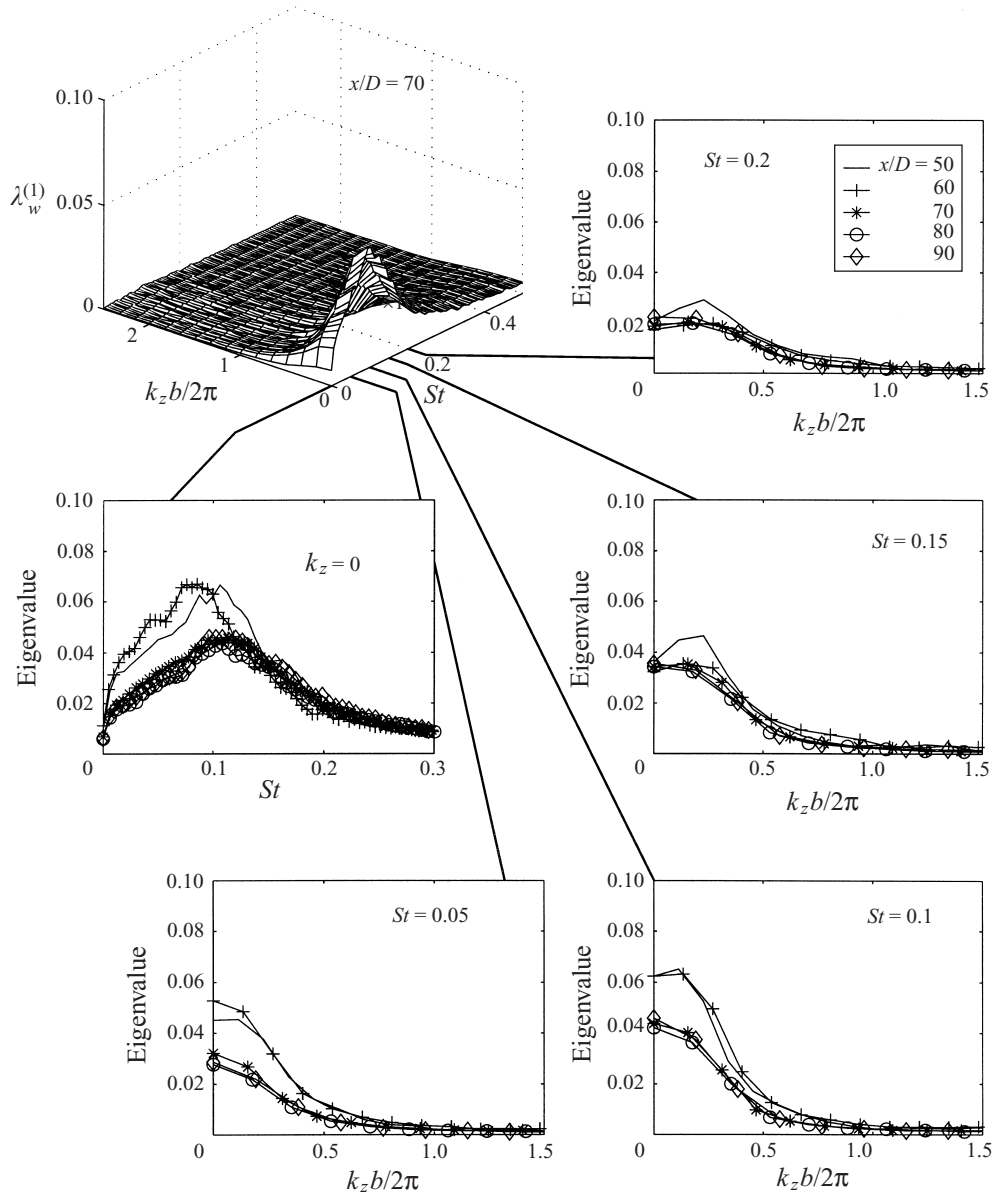
FIGURE 26. Scaled eigenvalues $\tilde{\lambda}_v^{(1)}(St, k_z; x/D)$ for the first v-mode.

position. Alternatively, we may slice the surfaces at selected k_z and compare their variation with Strouhal number at each streamwise location. Both approaches are taken in the results presented next.

Figure 25 presents the scaled mode 1 u-component eigenvalues. For reference, the scaled eigenvalue distribution in $(St, k_z b/2\pi)$-space at $x/D = 70$ is shown in order to indicate the location of the 'slices' taken for the associated plots. The figure shows the variation of the planar mode ($k_z = 0$) eigenvalues, $\tilde{\lambda}_u^{(1)}$, with St for $50 \leqslant x/D \leqslant 90$. In addition, the variation of $\tilde{\lambda}_u^{(1)}$ with $k_z b/2\pi$ is shown for four representative values of St over the same streamwise locations. This figure shows quite convincingly that

FIGURE 27. Scaled eigenvalues $\tilde{\lambda}_w^{(1)}(St, k_z; x/D)$ for the first w-mode.

the scaled u-component eigenvalue distribution becomes self-similar for $x/D > 50$ as evidenced by the congruence of the scaled profiles at the different x/D stations. The reader is invited to compare the scaled planar mode eigenvalue $\tilde{\lambda}_u^{(1)}$ variation with St shown in figure 25 with the unscaled version shown previously in figure 24(*b*). The effect of the similarity scaling in collapsing the eigenvalues at the various streamwise locations is obvious.

Figure 26 shows a similar representation of the scaled mode 1 v-component eigenvalues, $\tilde{\lambda}_v^{(1)}$. The variation of the planar mode ($k_z = 0$) eigenvalues with St for selected streamwise locations is shown to exhibit similarity. In addition, the variation with
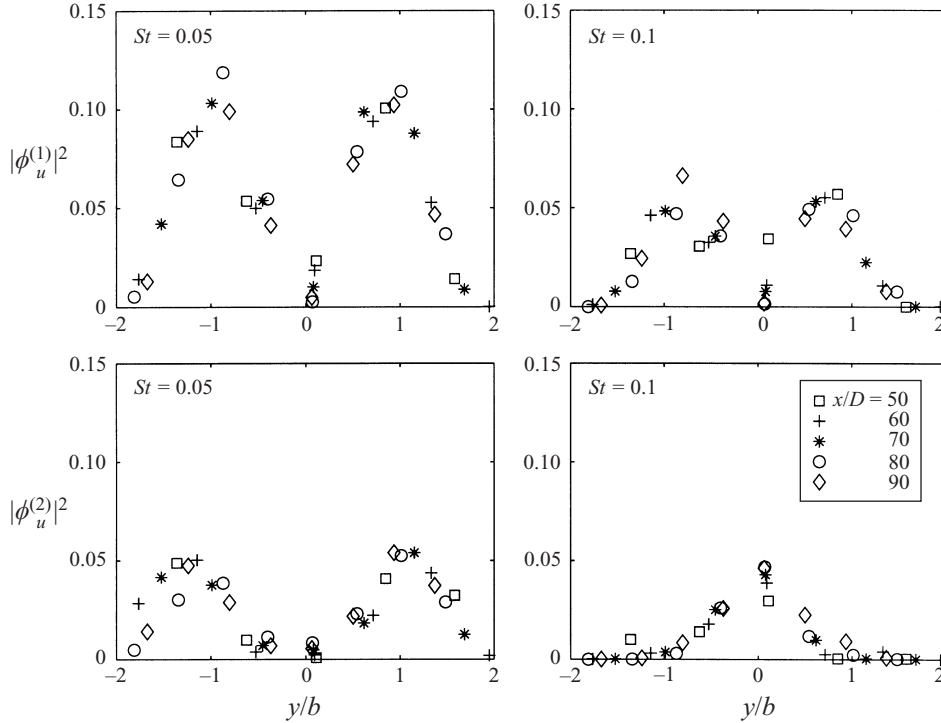
FIGURE 28. Scaled eigenfunctions $|\phi_u^{(n)}(y/b, St, k_z = 0; x/D)|^2$, $n = 1, 2$ for the u-mode.

span-wise wavenumber $k_z b/2\pi$ for selected St also exhibits collapses for the various x/D locations shown. Figure 26 shows that the v-component mode 1 eigenvalues exhibit similarity scaling for $x/D \geqslant 50$.

The scaled w-component mode 1 eigenvalues are shown in figure 27. This figure also shows evidence of self-similar behaviour for $\tilde{\lambda}_w^{(1)}$. However, unlike the u- and v-components, significant differences in the eigenvalue profiles remain apparent at $x/D = 50$ and 60. These data suggest that self-similar behaviour for the w-component eigenvalues occurs only for $x/D > 60$.

Although not presented here, the scaled eigenvalues associated with higher u-, v-, and w-component modes were also found to exhibit a collapse similar to that documented for mode 1. The reader is referred to Gordeyev (1999) for a full presentation of these results.

In order to assess the self-similarity of the scaled POD eigenmodes, cross-stream profiles at each streamwise location may be compared for given values of St and $k_z b/2\pi$. Such comparisons were made for numerous combinations of St and k_z and a sample of representative results is presented here. Figure 28 presents $|\phi_u^{(1)}(y/b; St, k_z = 0, x/D)|^2$ and $|\phi_u^{(2)}(y/b; St, k_z = 0, x/D)|^2$ for $St = 0.05, 0.1$ and $50 \leqslant x/D \leqslant 90$. These results illustrate the self-similarity in cross-stream u-component eigenmode shape that was found to characterize the other combinations as well.

Figure 29 presents similar results for the v-component eigenmode profiles. Again the comparison is shown for the planar mode, $k_z = 0$, with $St = 0.05, 0.1$. The self-similarity in v eigenmode profile shape is again readily apparent.

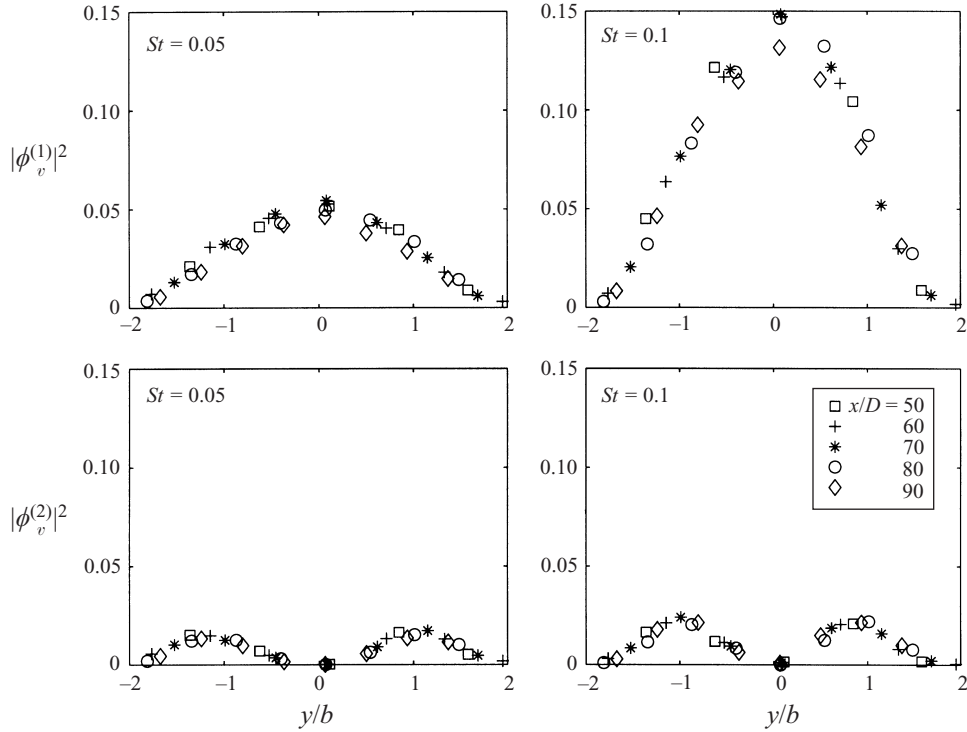Although not presented here, the scaled w-component eigenmode cross-stream

FIGURE 29. Scaled eigenfunctions $|\phi_v^{(n)}(y/b, St, k_z = 0; x/D)|^2$, $n = 1, 2$ for the v-mode.

profiles were also found to exhibit similarity scaling (except at $x/D = 50, 60$ as noted previously).

3.5. *POD results from the single-rake experiment*

As noted earlier, we consider the two-rake implementation of the POD the primary experiment and the more proper way of exploring the structure of the planar jet. This method provides eigenmodes and eigenvalues that exhibit an explicit dependence on spanwise wavenumber, k_z. However, a single-rake implementation of the POD was also performed in support of the primary experiment as described in §2.3. This was motivated by the fact that previous investigations in the planar jet have utilized two-point correlations confined to a single (x, y)-plane. In addition, the single-rake implementation allows a larger number of probes to be placed in the inhomogeneous direction and thereby enables eigenmode resolution issues to be addressed.

In this section the single-rake POD modes $\psi_\alpha^{(n)}(y/b; St)$ with corresponding eigenvalues $\mu_\alpha^{(n)}(St)$ as computed from (2.28) for the diagonal terms $S_{\alpha\alpha}$ are presented and compared to results from the two-rake experiment. Note that in the single-rake experiment the resulting eigenfunctions are not explicit functions of spanwise wavenumber k_z but depend only on Strouhal number, St, and the inhomogeneous spatial coordinate y. Since the one-rake experiment does not resolve the spanwise direction, the resulting POD modes will represent a weighted sum of the two-rake POD modes previously presented.

Figure 30(a) presents $|\psi_u^{(1)}(y; St)|^2$ and $|\psi_u^{(2)}(y; St)|^2$ obtained at $x/D = 70$. The associated eigenvalues $\mu_u^{(1)}(St)$ and $\mu_u^{(2)}(St)$ are presented in figure 30(b). A cross-stream asymmetry in both eigenmodes is apparent from figure 30(a). Note, in particular,
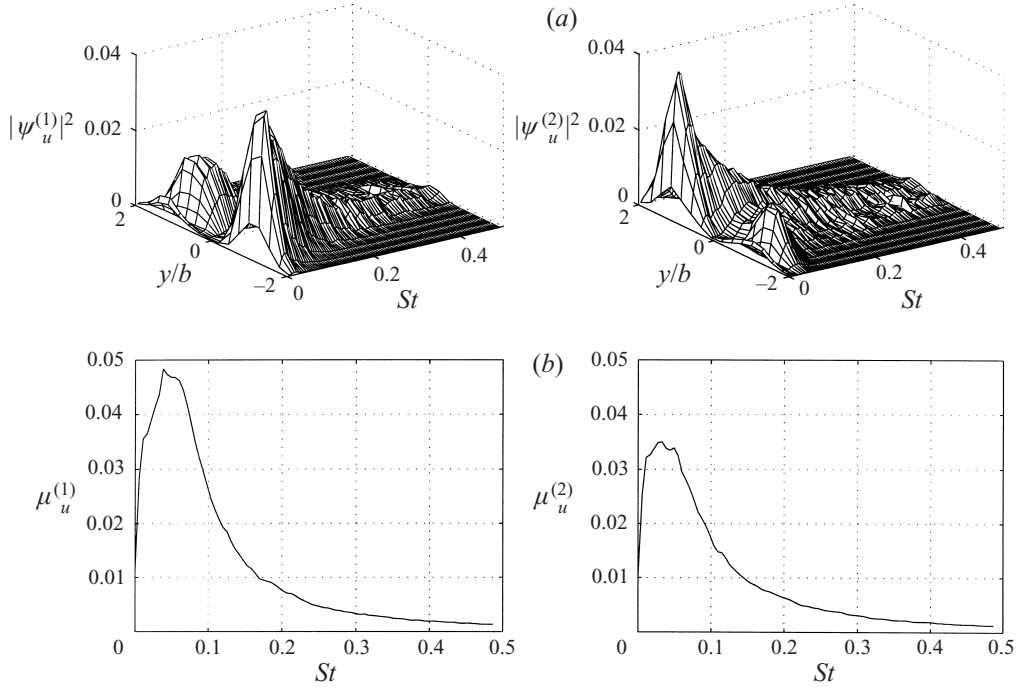
FIGURE 30. (a) The first two single-rake u-modes $\psi_u^{(n)}(y, St; x/D)$ with (b) the corresponding eigenvalues $\mu_u^{(n)}(St; x/D)$, $n = 1, 2$ at $x/D = 70$.

that values of $|\psi_u^{(1)}|^2$ are greater for $-y$ than for $+y$. The opposite is true for $|\psi_u^{(2)}|^2$. Recall from the two-rake POD results that the first two u-component eigenmodes also exhibited an identical cross-stream asymmetry *for non-zero spanwise wavenumbers*. This may be seen by comparing figure 30(a) with figures 21(b–d) and 22(b–d). Since the single-rake results presented here represent a weighted sum over all spanwise wavenumbers, the cross-stream asymmetry is an expected consequence of the contribution of the non-zero k_z modes. Similarly comparison of figure 30(a) with figures 21(b) and 22(b) clearly demonstrate that *single-rake measurements do not properly capture planar modes*. Figure 30(b) shows that the peak eigenvalues $\mu_u^{(1)}$ and $\mu_u^{(2)}$ occur at $St = 0.04$ and $St = 0.03$, respectively. These values are quite similar to those obtained in the two-rake experiment.

The v-component eigenmodes $|\psi_v^{(1)}(y, St)|^2$ and $|\psi_v^{(2)}(y, St)|^2$ are presented in figure 31(a) and both are observed to be symmetric in y. This is expected since the first (as shown in figure 23) and second POD modes from the two-rake experiment are also both symmetric in y. Note, however, that there are differences in the mode shapes between the two experiments. For example figure 31(a) shows the $|\psi_v^{(1)}(y, St)|^2$ mode shape to exhibit a broader peak near the jet centreline than is shown in figure 23(b). This difference is most likely due to the contribution of non-zero spanwise wavenumber modes. Figure 31(b) shows that peak eigenvalues $\mu_v^{(1)}$ and $\mu_v^{(2)}$ occur at $St = 0.09$ and $St = 0.07$, respectively.

4. Discussion

The energy content of the POD modes as expressed through their respective eigenvalues show rapid convergence with mode number. The v-component POD
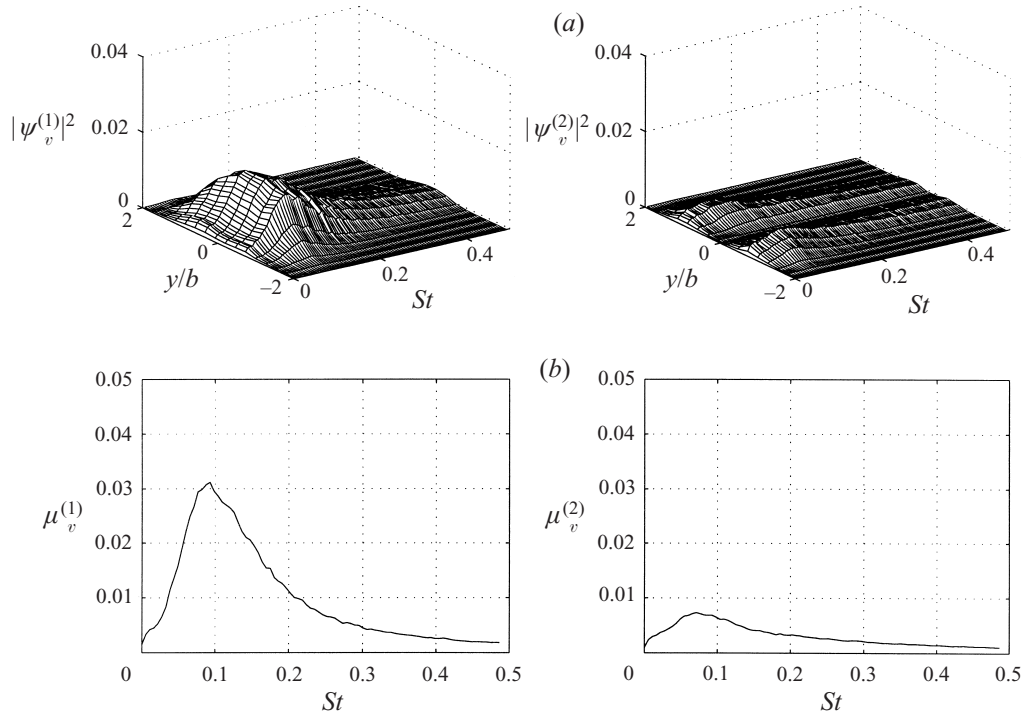
FIGURE 31. (*a*) The first two single-rake *v*-modes $\psi_v^{(n)}(y, St; x/D)$ with (*b*) the corresponding eigenvalues $\mu_v^{(n)}(St; x/D)$, $n = 1, 2$ at $x/D = 70$.

mode converges particularly rapidly with 61% of the large-scale *v*-fluctuation energy contained in mode 1 while the first three modes capture nearly 90%. The energy convergence of the *u*- and *w*-component modes is less rapid but still the first four modes each contain 85% and 80% of their respective large-scale fluctuation energy. These results are encouraging and suggest the potential for using the experimentally obtained POD modes in conjunction with Galerkin projection as the basis for obtaining a dynamical-system-based model of the coherent structure dynamics in the self-similar region of the turbulent planar jet. Of course there still exists energy transfer from the large resolved modes to small unresolved dissipative scales that must be accounted for. This interaction can be parametrically described by a model like the Heisenberg spectral model for isotropic turbulence (see Aubry *et al.* 1988).

Consistent with the theoretical predictions of Ewing (1995) which show that the correlation tensor admits self-similar solutions, the scaled POD eigenvalues and eigenmodes in the turbulent planar jet are shown to exhibit strong evidence of self-similarity. In particular, suitably scaled *u*-, *v*- and *w*-component POD modes and eigenvalues exhibit self-similar behaviour by $x/D = 60, 50$ and 70, respectively. Recall that measured second-order turbulence moments were observed to be self-similar for $x/D \geqslant 50$. The self-similarity of the POD modes is a sufficient condition to indicate that the average coherent structure in the turbulent planar jet scales in accord with the requirements for global flow field similarity. The self-similar behaviour of the POD modes is also consistent with previous observations which show that integral spatial macroscales obtained in the similarity region of the jet are proportional to the local mean velocity half-width.

The inability to perform direct measurements of the velocity cross-correlation

matrix for cases involving streamwise probe separations (due to probe wake interference) makes analysis of the streamwise coordinate problematic. Almost all existing approaches to the experimental investigation of jet dynamics are based on the assumption that the flow is homogeneous in the streamwise direction (i.e. the flow is assumed to be locally parallel). This assumption requires the use of Taylor's hypothesis and the streamwise evolution is then approximated through the local temporal evolution which is much easier to obtain experimentally. Physically this is equivalent to imposing wall-like boundary conditions on the jet which prevent it from spreading. Locally this approximation seems reasonable since in the self-similar region the spreading rate of the jet $\mathrm{d}b/\mathrm{d}x \approx 0.1$. One then expects this approximation to be locally dynamically similar to the real flow. While it may be suitable for examination of local dynamics, it is certainly not appropriate for dealing with the global dynamics of the jet. The question then arises as to whether the observed self-similar behaviour of the POD eigenmodes and eigenvalues may be exploited to provide an alternative approach to handling the streamwise coordinate. It is well known that self-similar behaviour in fluid mechanics considerably simplifies flow field modelling. Since the results of this paper indicate that the large-scale jet dynamics is self-similar, this suggests the possibility that the governing equations can be rewritten in self-similar coordinates whereupon the streamwise direction will become truly homogeneous. Unfortunately when this is done, time then becomes an inhomogeneous coordinate. Consequently, there does not appear to be a clear advantage of one approach over the other and the problem of how to properly deal with the inhomogeneous streamwise coordinate in modelling the flow remains open.

Even without a full dynamic reconstruction of the flow field structures in physical space, several characteristics regarding the time-averaged structure in the turbulent planar jet may be gleaned from examination of the POD modes presented in this paper. The results from the two-rake experiment indicate that the self-similar large-scale structure in the planar jet is three-dimensional in nature. However, it is natural, given the geometry of the flow field, to question whether some portion of this underlying structure can be approximated as planar. From the results presented here the answer seems to be yes. The results suggest that the flow supports a planar structure aligned in the spanwise direction ($k_z = 0$) as well as an essentially three-dimensional structure with asymmetrical shape in the y-direction and pseudo-periodically distributed in the spanwise direction. In particular, modal eigenvalue distributions in (k_z, St)-space indicate that a substantial fraction of the energy associated with the u-component POD modes and nearly all the energy associated with the v-component POD modes are due to an essentially planar component of the large-scale structure that extends in the spanwise direction. That is, most of the u- and v-component energy is associated with $k_z = 0$ and falls off quite rapidly for $k_z > 0$. The eigenvalues also exhibit a well defined peak in St with tails extending to somewhat higher values of St. This suggests that the planar structure is nearly periodic and may also exhibit an intermittent behaviour. This planar structure is reminiscent of the 'spanwise roller' structures noted by Mumford (1982) using a pattern recognition method. Measurements of Φ_{uv} indicate that large-scale Reynolds stress $\overline{u'v'}$ is governed largely by this planar component of the flow structure.

As noted earlier, the implementation of the POD presented in this paper is based on the diagonal elements of the cross-spectral matrix and neglects information contained in the off-diagonal terms. This was done in order to examine the self-similarity of the POD modes without implementing a Taylor's frozen field approximation in order to obtain the required Φ_{vw} term for the solution of (2.7). However, for the planar mode
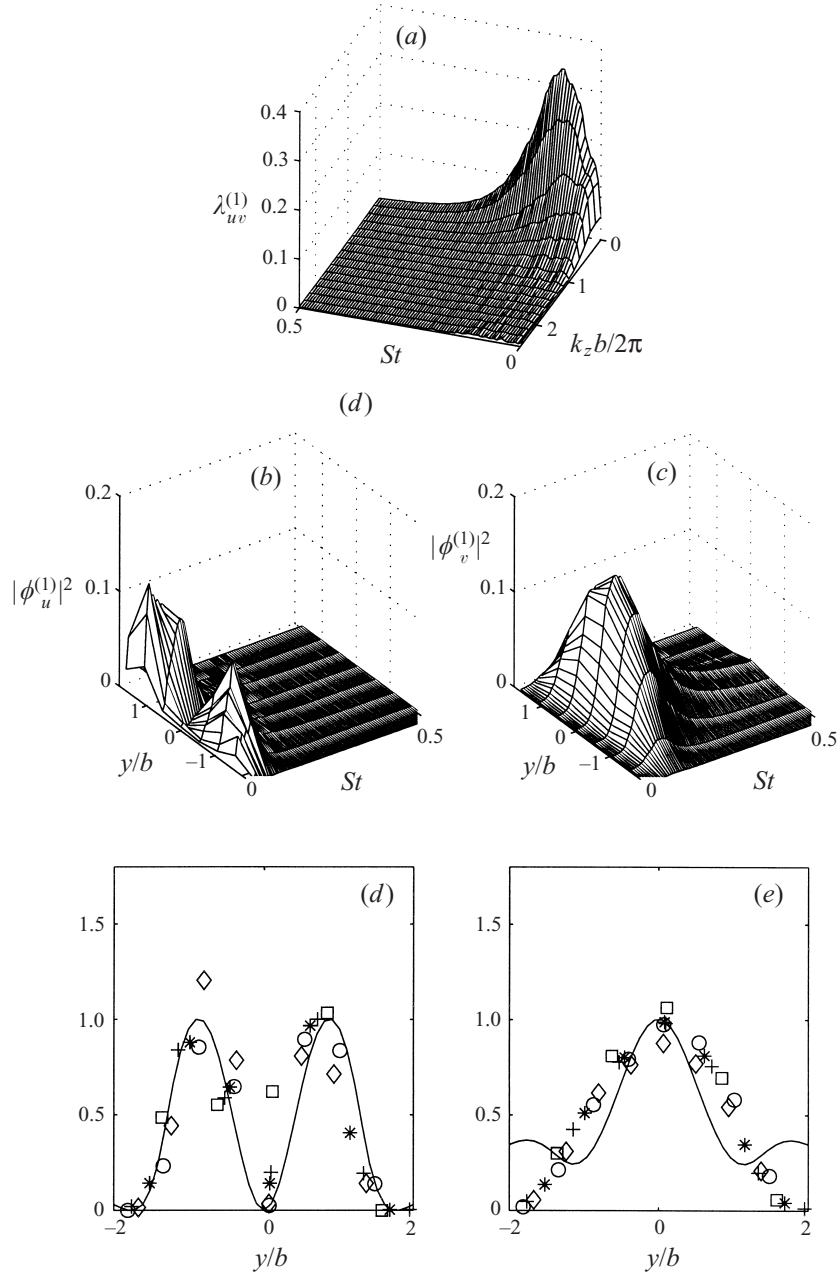
FIGURE 32. The planar u, v-mode at $x/D = 70$: (*a*) Eigenvalue $\lambda_{uv}^{(1)}(St; k_z)$, (*b*) u-eigenmode $|\phi_u^{(1)}(y, St, k_z = 0)|^2$, (*c*) v-eigenmode $|\phi_v^{(1)}(y, St, k_z = 0)|^2$, (*d*) Normalized u-modes $|\phi_u^{(1)}(y, St = 0.09, k_z = 0, x/D)|^2$ for several x/D (symbols) and the linear instability u-mode (solid line), (*e*) Normalized v-modes $|\phi_v^{(1)}(y, St = 0.09, k_z = 0, x/D)|^2$ for several x/D (symbols) and the linear instability v-mode (solid line). For meaning of symbols see figure 28.

$w' = 0$ and therefore this mode can be restored from (2.7), with $\alpha, \beta = u, v$ only. Thus, the planar POD mode is based upon Φ_{uu}, Φ_{vv} and the off-diagonal term Φ_{uv}. The resulting first POD eigenmode $\phi_\alpha^{(1)}(y, St, k_z = 0)$, $\alpha = u, v$ and associated eigenvalue $\lambda_{uv}^{(1)}(St, k_z)$ are presented in figure 32. Note that now the eigenvalue is the same for

both the u- and v-component POD modes. Recall that the diagonal elements Φ_{uu} and Φ_{vv} are dominant with respect to Φ_{uv}. Therefore, the POD modes obtained from solution of (2.7) shown in figures 32(b) and 32(c) compare quite favourably with those shown in figures 21 and 23 which result from the diagonal terms only (3.2). Note that the combined eigenvalue $\lambda_{uv}^{(1)}$ shown in figure 32(a) peaks at $St = 0.09$ while $\lambda_u^{(1)}$ and $\lambda_v^{(1)}$ peak at $St = 0.05$ and $St = 0.1$, respectively. It is interesting to note that the peak Strouhal number for the planar mode compares quite well with the Strouhal number corresponding to the jet 'flapping frequency' (1.1) reported in earlier studies of the planar jet.

The inviscid linear stability of the mean flow profile of figure 2(a) for spatially growing disturbances was examined by solution of the Rayleigh equation. This profile admits two modes of instability: a symmetric mode with respect to the jet centreline (i.e. symmetric in u', antisymmetric in v') and an antisymmetric mode (antisymmetric in u', symmetric in v'). Comparison of spatial growth rates indicates that the antisymmetric mode should dominate. The eigenvalue analysis gives $St = 0.06$ for the most unstable antisymmetric mode. The cross-stream variation of the squared modulus of the u- and v-eigenmodes obtained from the solution of the Rayleigh equation (for the most unstable antisymmetric mode) is compared with the first u- and v-component planar POD modes in figures 32(d) and 32(e). The eigenmodes represent the cross-stream variation of the spatially most unstable mode obtained under the assumption of a small linear perturbation of the parallel mean flow. In contrast, the POD modes represent the cross-stream shape of the dominant planar structures in the turbulent jet. In order to facilitate comparison of their shapes both have been normalized by their respective cross-stream spatial integrals. It is apparent from figure 32(d,e) that the eigenmodes resulting from the stability analysis bear a clear resemblance to the cross-stream shape of the first u- and v-component planar POD modes. This provides some evidence (although not proof) that the origin of the planar mode may lie in the local stability of the mean flow. This suggests a mechanism in which fluctuation energy is continuously provided at the appropriate local bandwidth for the sustenance of the coherent structure. This combined with the nearly inviscid nature of the largest scales of motion may explain the constant relative energy of the POD eigenmodes with streamwise distance.

The POD results also indicate an essentially three-dimensional component of the flow structure. This is apparent from examination of the changing character of the cross-stream u- and w-component POD mode shapes with increased k_z. The eigenvalue distributions for the u- and w-component modes both show significant energy content for $k_z > 0$. In each case, however, the modal amplitudes are very small for $k_z b/2\pi \geqslant 1$. This suggests a lower limit for the spanwise extent of the structure as $L_z \geqslant b$. That is, for the three-dimensional part of the structure, its minimum local spatial extent in the spanwise direction is of order b. Spanwise large-scale fluctuations appear associated with this three-dimensional structure. That there is significant $\overline{u'w'}$ coupling in the jet indicates that large-scale three-dimensional structures are responsible, in part, for the streamwise fluctuations.

The observations reported here regarding the character of the time-averaged structure in the turbulent planar jet are reminiscent of those reported by Mumford (1982) who suggested the presence of two kinds of vortical structures in the flow. One type, a planar spanwise oriented roller seems to correspond to the planar mode observed in this study. A secondary structure involved streamwise vortices aligned with local mean strain rate. This is probably associated with the three-dimensional portion of the POD structure which is associated with $\overline{u'w'}$ correlation.

Comparison of the single- and dual-rake implementations of the POD presented in this paper demonstrate that measurements confined to a single (x, y)-plane are incapable of properly extracting the planar modes. Rather, the single-rake implementation results in modes that appear to be a weighted sum of modes corresponding to different spanwise wavenumbers. In effect POD measurements in a single (x, y)-plane exhibit aliasing from non-zero k_z modes. This result can be generalized to indicate that previous published measurements in the planar jet that are confined to a single (x, y)-plane are not truly representative of planar structure but must result from a superposition of multiple spanwise wavenumber modes.

More detailed information regarding the coherent structure topology and its dynamic behaviour requires its restoration in physical space and an implementation of the POD that utilizes the full cross-spectral tensor $\Phi_{\alpha\beta}$. We will approach this task by a combination of the POD, the continuous wavelet transform and a triple-x-wire rake arrangement. This is the topic to which we turn our attention in Part 2.

REFERENCES

ADRIAN, R. J. 1977 On the role of conditional averages in turbulent theory. In *Turbulence in Liquids: Proc. 4th Biennial Symposium on Turbulence in Liquids* (ed. G. Patteson & J. Zakin), pp. 322–332. Science Press, Princeton.

ADRIAN, R. J. 1979 Conditional eddies in isotropic turbulence. *Phys. Fluids* **22**, 2065–2070.

ANTONIA, R. A., BROWNE, L. W. B., RAJAGOPALAN, S. & CHAMBERS, A. J. 1983 On the organized motion of the turbulent plane jet. *J. Fluid Mech.* **134**, 49–66.

ANTONIA, R. A., CHAMBERS, A. J., BRITZ, D. & BROWNE, L. W. B. 1986 Organized structures in a turbulent plane jet: topology and contribution to momentum and heat transport. *J. Fluid Mech.* **172**, 211–229.

ARNDT, R. E. A., LONG, D. F. & GLAUSER, M. N. 1997 The proper orthogonal decomposition of pressure fluctuations surrounding a turbulent jet. *J. Fluid Mech.* **340**, 1–33.

AUBRY, N., HOLMES, P., LUMLEY, J. L. & STONE, E. 1988 The dynamics of coherent structures in the wall region of the turbulent shear layer. *J. Fluid Mech.* **192**, 115–175.

BENDAT, J. S. & PIERSOL, A. G. 1986 *Random Data*, 2nd Edn. Wiley Interscience.

BERKOOZ, G., HOLMES, P. & LUMLEY, J. 1993 The proper orthogonal decomposition in the analysis of turbulent flows. *Ann. Rev. Fluid Mech.* **25**, 539–575.

BONNET, J. P. & DELVILLE, J. 1996 General concepts on structure identification. In *Eddy Structure Identification* (ed. J. P. Bonnet). Springer.

BRADBURY, L. J. S. 1965 The structure of a self-preserving turbulent plane jet. *J. Fluid Mech.* **23**, 31–64.

BRETETON, G. J. 1982 Stochastic estimation as a statistical tool for approximating turbulent conditional averages. *Phys. Fluids* A **4**, 2046–2054.

BROWNE, L. W. B., ANTONIA, R. A. & CHAMBERS, A. J. 1984 The interaction region of a turbulent plane jet. *J. Fluid Mech.* **149**, 355–373.

CERVANTES, D. G. & GOLDSCHMIDT, V. W. 1981 The apparent flapping motion of a turbulent plane jet-further experimental results. *Trans. ASME: J. Fluid Engng* **103**, 117–126.

CITRINNITI, J. 1996 Experimental Investigation into the Dynamics of the Axisymmetric Mixing Layer Utilizing the Proper Orthogonal Decomposition. PhD dissertation, SUNY Buffalo.

CHU, H. C. 1993 An experimental study of nonlinear wave coupling and energy transfer characterizing the transition of a planar jet shear layer. PhD dissertation, University of Notre Dame.

DELVILLE, J. 1993 Characterization of the organization in shear layers via the proper orthogonal decomposition. In *Eddy Structure Identification in Free Turbulent Shear Flows* (ed. J. P. Bonnet & M. N. Glauser). Kluwer.

DELVILLE, J. 1994 Characterization of the organization in shear layers via the proper orthogonal decomposition. *Appl. Sci. Res.* **53**(3–4), 263–281.

DELVILLE, J., BELLIN, S. & BONNET, J. P. 1990 Use of the proper orthogonal decomposition in a plane turbulent mixing layer. In *Turbulence and Coherent Structures* (ed. O. Metais & M. Lesieur). Kluwer.

DELVILLE, J., UKEILEY, L., CORDIER, L., BONNET, J. P. & GLAUSER, M. 1999 Examination of large scale structures in a plane mixing layer. Part 1. Proper orthogonal decomposition. *J. Fluid Mech.* **391**, 91–122.

EVERITT, K. W. & ROBINS, A. G. 1978 The development and structure of turbulent plane jets. *J. Fluid Mech.* **88**, 563–583.

EWING, D. 1995 On multi-point similarity solutions in turbulent free-shear flows. PhD dissertation, SUNY at Buffalo, Amherst, New York.

FLORA, J. J. & GOLDSCHMIDT, V. W. 1969 Virtual origins of a free plane turbulent jet. *AIAA J.* **7**, 2344–2346.

GLAUSER, M. N. 1987 Coherent Structures in the Axisymmetric Turbulent Jet Mixing Layer. PhD dissertation, SUNY, Buffalo.

GLAUSER, M. N. & GEORGE, W. K. 1989 An orthogonal decomposition of the axisymmetric jet mixing layer. In *Turbulent Shear Flows 6* (ed. Y. C. Andre *et al.*). Springer.

GLAUSER, M. N. & GEORGE, W. K. 1992 Application of multipoint measurements for flow characterization. *Expl Thermal Fluid Sci.* **5**, 617–632.

GOLDSCHMIDT, V. W. & BRADSHAW, P. 1973 Flapping of a plane jet. *Phys. Fluids* **16**, 354–355.

GOLDSCHMIDT, V. W., YOUNG, M. F. & OTT, E. S. 1981 Turbulent convective velocities (broadband and wavenumber dependent) in a plane jet. *J. Fluid Mech.* **108**, 327–345.

GORDEYEV, S. V. 1999 Investigation of coherent structure in the similarity region of the planar turbulent jet using POD and wavelet analysis. PhD dissertation, University of Notre Dame.

GORDEYEV, S. V. & THOMAS, F. O. 2000 Coherent structure in the turbulent planar jet. Part 2. Structural topology via POD eigenmode projection. *J. Fluid Mech.* (submitted).

GUTMARK, E. & WYGNANSKI, I. 1976 The planar turbulent jet. *J. Fluid Mech.* **73**, 465–495.

HERZOG, S. 1986 The large scale structure in the near wall region of turbulent pipe flow. PhD dissertation, Cornell University.

HOLMES, P., LUMLEY, J. L. & BERKOOZ, G. 1996 *Turbulence, Coherent Structures and Symmetry.* Cambridge University Press.

KARHUNEN, K. 1946 Zur Spektraltheorie Stochasticher. *Prozessa Ann. Acad. Sci. Fennicae* **37**.

LOÈVE, M. M. 1955 *Probability Theory.* Van Nostrand.

LUMLEY, J. 1967 The structure of inhomogeneous turbulent flows. In *Proc. Intl Colloq. on the Fine Scale Structure of the Atmosphere and its Influence on Radio Wave Propagation* (ed. A. M. Yaglam & V. I. Tatarsky), pp. 166–178. Doklady Akademii Nauk SSSR, Moscow, Nauka.

LUMLEY, J. 1970 *Stochastic Tools in Turbulence.* Academic.

LUMLEY, J. 1981 Coherent structures in turbulence. In *Transition and Turbulence* (ed. R. E. Meyer), pp. 215–241. Academic.

MOUM, J. N., KAWALL, J. G. & KEFFER, J. F. 1983 Coherent structures within the plane turbulent jet. *Phys. Fluids* **26**, 2939–2945.

MUMFORD, J. C. 1982 The structure of the large scale eddies in fully developed turbulent shear flows. Part 1. The plane jet. *J. Fluid Mech.* **116**, 241–268.

OLER, J. W. & GOLDSCHMIDT, V. W. 1982 A vortex-street model of the flow in the similarity region of a two-dimensional free turbulent jet. *J. Fluid Mech.* **123**, 523–535.

THOMAS, F. O. & BREHOB, E. G. 1986 An investigation of large-scale structure in the similarity region of a two-dimensional turbulent jet. *Phys. Fluids* **29**, 1788–1795.

THOMAS, F. O & GOLDSCHMIDT, V. W. 1986 Structural characteristics of a developing turbulent planar jet. *J. Fluid Mech.* **163**, 227–256.

TSO, J. & HUSSAIN, A. K. M. F. 1989 Organized motions in a fully developed turbulent axisymmetric jet. *J. Fluid Mech.* **203**, 425–448.

UKEILEY, L. & GLAUSER, M. 1995 Dynamics of large-scale structures in a plane turbulent mixing layer. *Rep.* MAE-311. Department of Mechanical and Aeronautical Engineering, Clarkson University.

WEIR, A. D., WOOD, D. H. & BRADSHAW, P. 1981 Interacting turbulent shear layers in a plane jet. *J. Fluid Mech.* **107**, 237–260.